UNIVERSITY OF TURKU

Metalloporphyrin decorated rGO-TiO_2 composite for understanding electrochemical properties towards CO_2 reduction

Faculty of Science,

Department of Chemistry

Master's thesis

Master's Degree Programme in Materials Chemistry

Author: Adiba Farah

Supervisor(s): **Sachin Kochrekar, Carita Kvarnstrom**

22nd Deccember 2023

ABSTRACT:

Carbon dioxide (CO_2) significantly contributes to global warming and climate change. The excessive burning of fossil fuels to fulfil almost 80% of global energy demand is largely responsible for CO_2 emission. To alleviate the negative impact of CO_2 discharge, many researchers are exploring ways to convert CO_2 into value-added hydrocarbon (HC) fuels as an efficient solution for diminishing greenhouse gas emissions and developing sustainable sources of renewable energy. CO_2 electroreduction is a promising technology that involves the use of an electrocatalyst, that can facilitate the electrochemical reduction of CO_2 into green products that can provide a pathway towards a circular carbon economy.

This study focuses on synthesizing beneficial nano hybrid electrocatalysts and analysing their electrocatalytic properties for the effective electrochemical reduction of CO_2. Herein, metalloporphyrin is incorporated as a molecular cocatalyst with the TiO_2 (P25) and rGO (reduced graphene oxide) composite to enhance the electron transfer kinetics and electrochemical reduction activity of CO_2. This trio of GO-TiO_2 /metalloporphyrin catalysts was synthesized by performing the solvothermal process. The characterizations of the catalyst composites are analysed by performing several instrumental techniques such as Fourier-transform infrared (FTIR) spectroscopy, Raman spectroscopy, Thermogravimetric analysis (TGA), UV-visible spectroscopy, X-ray photoelectron spectroscopy (XPS) and X-ray diffraction (XRD) techniques. These spectroscopic techniques have provided valuable insights into the structure, morphology, and composition of the composite material. The electrochemical reduction performance of the prepared catalysts was assessed by performing cyclic voltammetry with rGO-TiO_2/TAPP, rGO-TiO_2/ Zn-TAPP and rGO-TiO_2/Ni-TAPP nano electrocatalyst coated on glassy carbon (GC) electrode.

Table of contents

ABBREVIATIONS

rGO Reduced graphene oxide.

GO Graphene oxide.

TiO_2 Titanium dioxide

CV Cyclic voltammetry

GC Glassy carbon

DI Deionized Water

$TBAPF_6$ Tetrabutylammonium hexafluorophosphate

TAPP Meso tetra (4-amino phenyl) porphyrin

Zn-TAPP Meso tetra (4-amino phenyl) Zinc porphyrin

Ni-TAPP Meso tetra (4-amino phenyl) Nickel porphyrin

Pt Platinum

Au Gold

KCL Potassium chloride

ACN Acetonitrile

DMF N, N-dimethylformamide

THF Tetrahydrofuran

CO_2 Carbon Di oxide

ECR Electrochemical Reduction

1 INTRODUCTION:

The present world is now confronting the negative consequences of extreme global warming in the disguise of drought, heatwave, and ocean acidification because of excessive amounts of greenhouse gas (GHG) discharged from different energy-driven sectors per annum [1]. CO_2 is the major contributor (74.4%) of the total discharged of these GHGs [2]. Based on many scientific studies it has been found that emitted CO_2 from fossil fuel combustion remains accumulated in the atmosphere for a longer period almost 100–160,000 years compared to other GHG emissions causing grave damage to the global environment [3]. It has been estimated that the burning of fossil fuels will produce more than 500 gigatons of CO_2 over the next few decades [4]. According to the global carbon budget report of 2022, CO_2 emission from fossil fuel combustion and industrialization like cement production has already reached a record high of 36.6 billion tons [5]. The amount of CO_2 released due to energy consumption jumped by 0.9%, or 321 Mt in 2022 [6]

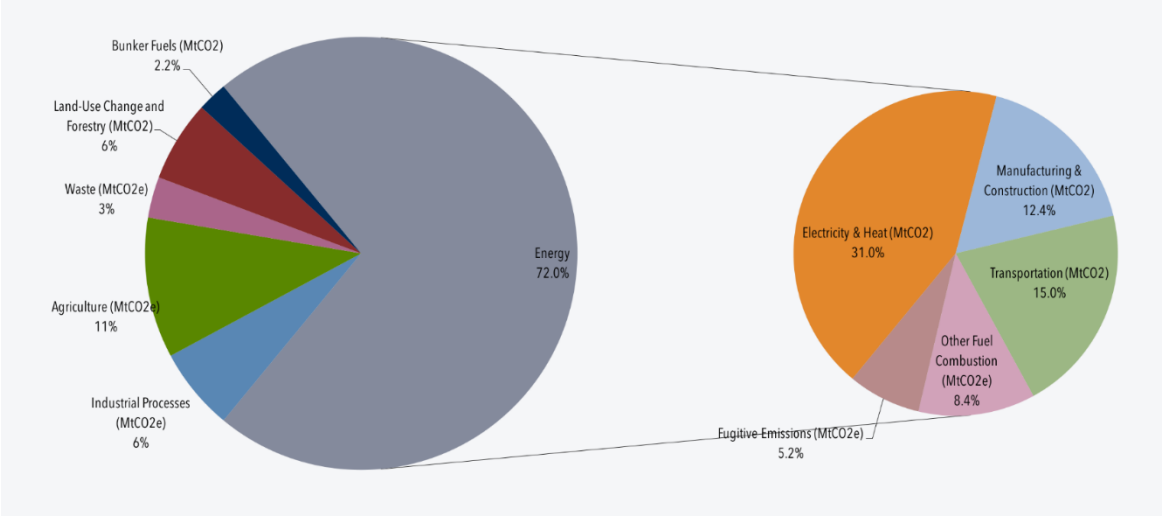

Figure 1: Global Primary sources of Green house Gas $MTCO_2e$ (Metric tons of carbon dioxide equivalent) emissions. (Climate Analysis Indicators Tool , World Resources Institute, 2017).

Since the middle of the 20th century, the rate of global energy consumption for transporting, heating and electricity is alarmingly accelerating to ensure the smooth growth of civilization and industrialization. To fulfill this existing demand of energy we are particularly reliant on fossil fuel-based energy resources.

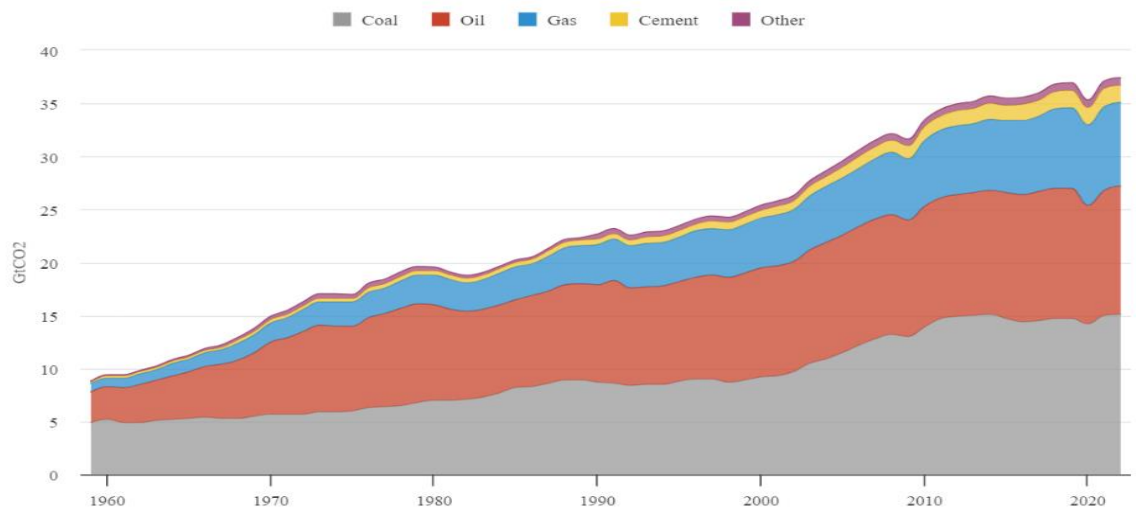

Figure 2. Global CO_2 emissions from energy combustion and industrial processes and their annual change, 1959-2022 (chart by Carbon Brief)

Unfortunately, the reservation of these nonrenewable (petroleum, coal, natural gas etc.) resources is limited and scarce. Subsequently, excessive use and the rapid depletion of these primary energy sources will cause the future generation to face a great energy crisis. To resolve these aforementioned issues, researchers have discovered alternative strategies like improving energy efficiency and replacing non-renewable energy sources with renewable sources such as harnessing renewable electricity from natural and low or non-carbon sources like solar PV, geothermal, wind generation, hydropower, nuclear etc. To produce clean and sustainable energy,converting CO_2 into high-value commodities and hydrocarbon fuels like carbon monoxide (CO), formate ($HCOO^-$) or formic acid (HCOOH), methane (CH_4), ethylene (C_2H_4), ethanol (C_2H_5OH), and other alcohols are also effective ways of decarbonizing the global energy supply [7], [8]. Several promising methods have been encountered theoretically and experimentally so far including thermochemical [9] biochemical [10] radiochemical [11], photochemical, photoelectrochemical [12] and electrochemical [13] reactions for efficient transformation of CO_2 into clean fuel. Comparatively, electrochemical CO_2 reduction reaction (CO_2RR) for chemical conversion of CO_2 has become a more widespread topic of scientific research because of several advantages among which are noteworthy mentioned 1) Reasonably powered by renewable sources such as the electricity force like solar, wind and nuclear energy to run the conversion preventing from producing any extra CO_2; 2) Less expensive equipment and ambient operating conditions like temperature and pressure 3) Chemical usage can be abated by recycling the electrolytes 4) The reaction pathways can be control effortlessly to

produce a desired product by changing and selecting an appropriate external potential, electrolyte and electrocatalysts [14].

But as CO_2 ERR is thermodynamically a sluggish kinetic process, to practical and successful implementation and commercialization of this process, the development of an active, selective, stable, and reasonably inexpensive electrocatalyst is inevitable. Numerous researchers have devoted many years to investigating and designing different types of electrocatalysts including metal electrodes, metal alloys, inorganic metal compounds, organic metal complexes and various others for efficient CO_2 electroreduction [15]

This thesis experiment aim is also synthesizing an efficient and environment-friendly hybrid electrocatalyst with Meso tetra 4-amino phenyl porphyrin(TAPP), Meso tetra 4-amino phenyl zinc porphyrin (Zn-TAPP)and Meso tetra 4-amino phenyl nickel porphyrin (Ni-TAPP) decorated on rGO- TiO_2 for utilizing it successfully for electrochemical reduction of CO_2.

1.1 METALLOPORPHYRIN

Over the last few decades, a wide variety of molecular catalysts that are mainly organic molecules like porphyrins [16], phthalocyanines [17] cyclam [18] and polypyridines [19] have been introduced and studied as potential catalysts for CO_2 reduction reactions. This molecular electrocatalyst is identified as different types of noble (i.e. Re, Rh, Ir, Ru, Os and Pd) or earth-abundant non-noble (Fe, Co, Ni, Mn, Cu, Zn) transitional metal-based complexes with macrocycle, porphyrin or phosphine ligands. Although non-noble metals have lately substituted noble metals for synthesizing different types of active metal complexes as they are less expensive and highly reaction active. For instance, Co, Fe, Ni, and Cu-porphyrin complexes have replaced the noble metal Platinum in H_2 generation reactions for better economical and workable options [20], [21], [22].

In our study, we have selected Meso tetra 4-amino phenyl porphyrin, TAPP, and two types of metal ions (Ni^{2+}, and Zn^{2+}) complexes of TAPP to hybridize with rGO- TiO_2 and synthesize a suitable electrocatalyst for CO_2ERR. Porphyrin metal complexes can efficiently transfer electrons in a catalytic system which can decrease the recombination of electron-hole pairs and can also broaden the absorption range [23].

Porphyrins are mainly N4 macromolecular, heterocyclic and highly conjugated 18π electron-containing compounds that are widely available in nature such as in chlorophylls and in heme or can be synthesized in the laboratory. Its capability to catalyse various oxidation reactions in biosystems and light harvesting capacity has given it the recognition of an environment-friendly bionic catalyst and active biological enzyme. The aromaticity of the porphyrin compounds with a large delocalized π-electronic system is the key reason for its semiconducting behavior and efficient electron transfer capability. The free base of porphyrin can be converted into metalloporphyrin by replacing the two inner pyrrole protons with a metal ion, shown in Figure 3. A great number of transitional metal porphyrin complexes are possible to produce by changing the side chains and core metal ions. The metal ion that is coupled with the porphyrin framework mainly determines the electron density of porphyrin rings. The addition of ligands or the introduction of electron-donating or electron-withdrawing groups in meso or β-positions can improve the overall catalytic performance, stability, and high selectivity of a metalloporphyrin in a variety of processes.

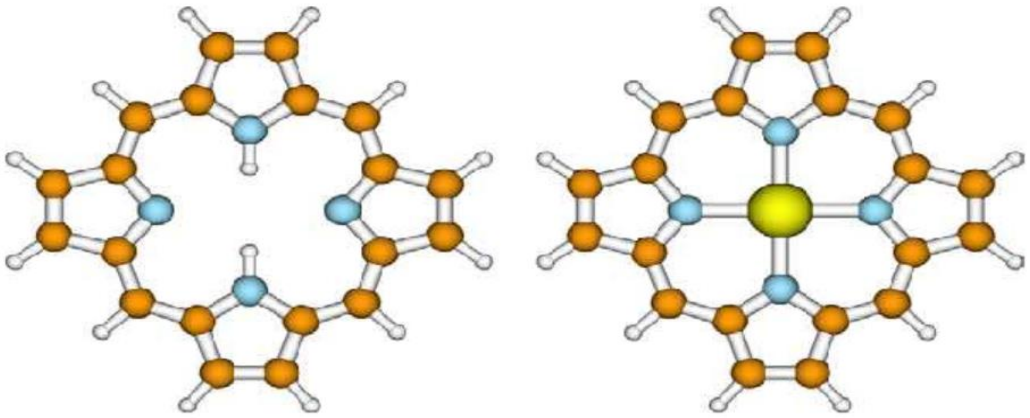

Figure 3: Typical structure of Porphyrin and Metalloporphyrin

Metalloporphyrin complexes as homogeneous catalysts face challenges like complicated preparation processes, reaction surroundings, difficulty in product separation, poor solubility in aqueous electrolytes and inactivation when far from the conductive electrode surface. On the contrary, the heterogeneous electrocatalyst of metalloporphyrin complexes shows better practical application by overcoming the mentioned drawbacks of the homogeneous form of catalyst. It can also control the chemical surroundings of the catalyst's active site by improving the catalytic performance and preventing the deactivation caused by dimerization and aggregation in a homogeneous process.

Porphyrin-based transition metal complexes are stable, affordable, readily functionalized, and possess exceptional tuneable optical, photophysical, and electrical properties and efficient energy transformation capability. Its semiconducting nature, high catalytic efficiency and selectivity have made them a promising catalyst in diversified applications including artificial photosynthesis, biometric chemistry, photodynamic therapeutic agents, molecular electronics, sensors, non-linear optics, charge separation in solar cell materials [24], [25], [26], [27], [28]. The facile structure and tunable oxidation state of metal centers of metalloporphyrin complexes have proven it a model catalyst for electro/photo catalytic water splitting [29], CO_2 reduction, O_2 reduction [30], nitrate reduction [31], hydrogen evolution [32] and other reactions in numerous studies. For effective energy conversion, immobilization of a metal into an organic framework (MOF) or covalent organic frame work (COF) or combination of both MCOFs, are being lately extensively explored by scientists because of the porous structure of the material that provides a higher number of active sites, stability and high specific surface area for an efficient catalytic activity like CO_2 reduction [33].

Around 1988, Savéant et al. reported the first electrochemical reduction of CO_2 by applying iron tetraphenylporphyrin complex (Fe-TPP, where TPP = 5,10,15,20- tetraphenylporphyrin) as a catalyst and obtained CO as a major product. After that, Saveant and his coworkers has studied Fe porphyrin complexes further for CO_2 reduction extensively [34], [35], [36]. Idan Hod et al., opted for a heterogeneous electrocatalyst by synthesizing Fe porphyrin-based MOF (metal−organic framework) thin films-525 that contains TCPP [meso-tetra(4-carboxyphenyl)porphyrin] linkers and hexa-zirconium nodes. In this experiment, MOF-525 acts as a catalyst immobilizer that has provided good molecular-scale porosity and excellent chemical stability for the electrocatalytic reaction with ∼100% faradic efficiency of the CO and H_2 mixed products with an overpotential of ∼650 mV for CO_2 electrochemical reduction [37].

Cobalt (Co) porphyrin complexes have also been studied as a molecular catalyst under both homogeneous and heterogeneous conditions for CO_2 reduction reactions. Dr Xin-Ming Hu and his colleagues have approached both heterogeneous and homogeneous (organic medium - DMF)conditions for CoTPP (Cobalt meso-tetraphenylporphyrin) catalyst.But compare to homogeneous state they observed a high catalytic activity with a low overpotential , good current density and FE >90% to produce CO from CO_2 electrolysis reaction under heterogeneous conditions in the presence of aqueous solution. In heterogenous form, CoTPP catalyst was immobilized on a CNT via adsorption. The TON turnover number) 1118 and TOF (turnover frequency) 280 h^{-1}were also 300 times higher than in the homogeneous process of the same catalyst [38].

Song Lin et al. synthesized Co(II)-porphyrin-based covalent organic framework (COF) for an aqueous electrochemical reduction of CO_2. 5,10,15,20-tetrakis(4 aminophenyl)porphinato]cobalt, Co(TAP), was used for the catalyst framework and the COF powders were deposited on porous, conductive carbon fabric for the electroreduction. A high selectivity for CO formation (FE=90%) and turnover numbers 290,000, with an initial turnover frequency of 9400 $hour^{-1}$ at –0.55 V overpotential was detected. It has been observed that the incorporation of cobalt porphyrin complex into COF has 26-fold increased the overall catalytic activity of the molecular Co catalyst [39] .

1.2 TITANIUM DIOXIDE (TiO_2)

Titanium dioxide (TiO_2 or titania) is one of the most popular transition metal oxides and n-type semiconducting material. It has received a lot of interest ever since Fujishima and Honda utilized it successfully for water photolysis in 1972 [40]. Compared to other metal oxides, nanostructured TiO_2 (diameter > 100 nm) is prefered for use in versatile reactions because of its outstanding physical and chemical qualities such as stable chemical structure, non-toxicity, economical, higher specific surface area, photoactivity/light absorption and greater dispersibility. Furthermore, it has possessed other abilities like enhanced porosity, biocompatibility, excellent optical properties, redox and strong oxidizing capability.The presence of bulk vacancies for oxygen and efficient electron/hole separation are the focal reasons for its electrical conductivity [41], [42].

Nanoparticles, NP, of TiO_2 are frequently applied in food, cosmetics, pharmaceuticals [43], paints, plastics, self-cleaning coating [44] and medical therapies [45] because of their improved efficiency and exceptional adjustable properties. In the last few decades, its application has widely intensified in high-tech diversified fields mostly in environmental and energy-related areas like water splitting for producing H_2 [46], solar cells, sensors, supercapacitors, photocatalysis, photovoltaic, air purification, antibacterial, dye degradation and water desalination [47], and in Li-ion batteries [48]. TiO_2 NPs can be synthesized by following a number of procedures including the sol-gel method, chemical vapour deposition, mechanical alloying, 3D printing, hydrothermal method green synthesis etc. [49].

The properties of this nanomaterial are largely influenced by its size, shape, surface morphology and crystal phase. Anatase, rutile and brookite are the main crystallographic structures of TiO_2 struvture shown in Figure 4. Anatase has better photocatalytic ability than others due to its excellent electron mobility, electron affinity, and visible light transmission [50]. Rutile is thermodynamically more stable and has been usually used as an effective light-scattering material for dye/semiconductor-sensitized solar cells as it has a high refractive index [51]

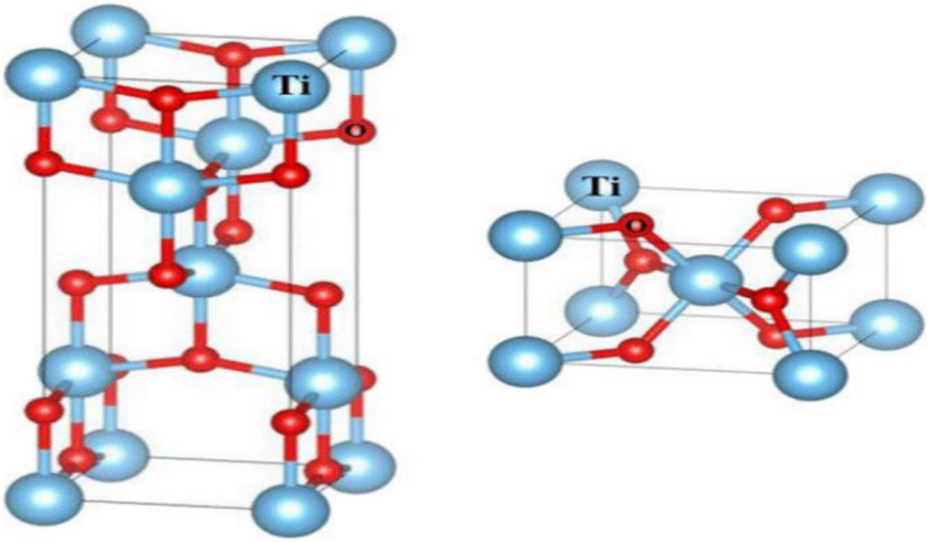

A) B)

Figure 4: Unit cells of A) anatase TiO_2 and B) rutile TiO_2. Large light-blue and small red spheres are Ti^{4+} and O^{2-} ions, respectively [52] .

The usage of TiO_2 as a heterogeneous catalyst support or co-catalyst in CO_2 electroreduction has been reported in a limited number of studies so far. In some of these studies, it has been noted that the mesoporous structure of TiO_2 NPs and large surface area displayed strong redox abilities and chemical stability that aids in carrying electrons in various catalytic reactions like CO_2 reduction reactions. Furthermore, the surface of TiO_2 has the adsorption capability of CO_2 that helps to stabilize CO_2 reduction intermediates and to decrease the overpotential [53]. Though TiO_2 is the most commonly used photo electrocatalyst in catalytic reactions, its functionality is highly constrained because of the fast recombination of the photo-induced electron-hole pairs and low adsorption of visible light. This is due to the wide band gap (rutile 3.0 eV and anatase 3.2 eV) averting it from being stimulated by anything other than UV light which is only a small fraction (5%) of solar light. The effective strategies for overcoming the

limitations of TiO_2-based photocatalysts are categorized by different scientists as follows: (i) Design of nanostructured TiO_2-based catalysts, (ii) modification of TiO_2 facial properties, and (iii) Usage of cocatalysts for TiO_2 photocatalysts. Different types of metal and noble metal, nonmetal, photosensitization, semiconductor composite, and carbon-based materials coordinated with TiO_2 as cocatalyst have so far demonstrated successful results by widening the band gap of TiO_2 to the visible range and preventing the recombination of electron/hole pair [54].

In our study, we have used P25 mixed phase of anatase-rutile:70–80 % anatase and 20–30 % rutile) as a cocatalyst for synthesizing a composite catalyst for CO_2ERR. P25 is commercially available popular semiconductor photocatalyst that possesses high photocatalytic activity due to interface electro-transmission ability, greater ionic charge separation and longtime electro-hole separation [55].

Jing Yuan et al. investigated Cu/TiO_2 NP anchored onto N-doped graphene, NG, for CO_2 electro reduction to different alcohols. Cu/TiO_2 /NG heterogeneous catalyst has shown excellent stability and dual catalytic ability as it produced both methanol with FE 19.5% at a potential of −0.20 V vs. the reversible hydrogen electrode (RHE), and ethanol with a higher FE up to 43.6% (at −0.75 V vs. RHE) compared to Cu/NG with 12.7% FE for methanol (at −0.20 V vs. RHE) and 24.1% FE for ethanol (at −0.75 V vs. RHE). Also, Cu/TiO_2/NG demonstrated (at −0.20 V vs. RHE) a larger partial current density, J (0.061 mA/cm^2) for methanol compared to Cu/NG (0.041 mA/cm^2) and a 2.06-fold higher J on Cu/TiO_2/NG (at −0.75 V vs. RHE) than that on Cu/NG for ethanol of CO_2 reduction. This indicates that the presence of TiO_2 has increased the overall electrocatalytic activity of Cu/TiO_2 /NG catalyst by showing a high efficiency and low overpotential for CO_2 electrocatalytic reduction in contrast to the Cu/NG catalyst [56].

In a recent experiment conducted by M. Nur Hossain and his team a TiO_2/Au nanocomposite was used for electrochemical reduction of CO_2 towards multiple hydrocarbons. Usually, Au-based nanomaterials have successfully produced CO in an aqueous solution for CO_2 electro reduction [57] but the nanocomposite TiO_2/Au synthesized by galvanic replacement reaction have produced highly energetic gas products CO and CH_4 and liquid products like $HCOO^-$, CH_3COO^-, CH_3OH, and CH_3CH_2O (formate, acetate, methanol, and ethanol) from the CO_2 electroreduction at different cathodic potentials. Au^{3+} ions were reduced and the Au thin layer was deposited on to TiO_2 NPs. The presence of TiO_2 has improved the catalytic performance of the TiO_2/Au nanocomposite electrode catalyst compared to polycrystalline Au with the instant current efficiency (ICE) 67.2 and FE 67.36% at−0.5 V (vs RHE) in a CO_2-saturated

0.1 M $NaHCO_3$ solution by decreasing the overpotential for CO_2 reduction and improving the reaction stability at the intermediate stage [58].

1.3 GRAPHENE, GRAPHENE OXIDE, and REDUCED GRAPHENE OXIDE

A single layer of graphene is one of the thinnest, strongest and lightest two-dimensional (2D) materials composed of sp^2 hybrid carbon atoms with a layered hexagonal honeycomb structure. It's the elementary unit of many other carbonic materials with different morphologies like fullerenes wrapped into 0D structure, carbon nanotubes rolled into 1D structure and stacked 3D graphite.

In 2004, Novoselov and Geim successfully separated a single layer of graphene by repeated peeling from bulky graphite. Since then graphene has emerged as a blessing for the 21st century in the field of technology because of its distinct lattice structure, morphological features, and C-C bond (~ 1.42 Å) that offers excellent chemical stability, bio compatibility, good electron transfer capability, exceptional optical transparency (97.4%) and distinct thermal conductivity ($5000 Wm^{-1}K^{-1.}$). Moreover, the strong planar σ bonds provides its astounding mechanical properties that include a break strength of 42 N m^{-1}, Young's modulus of 1.0 TPa, and tensile strength of 130 GPa. The presence of π bonds is mainly responsible for its excellent electrical capabilities. Besides, the large surface area (~ 2630 m^2 /g), zero gaps between valence and conduction bands, rapid electron transfer rate (200,000 cm^2 /Vs, 200 times higher than silicon) and capability to be functionalized variously are the key reasons for its widespread application in environment, biomedicine, electrochemical and energy-related fields [59], [60], [61].

The two major synthesis methods of graphene are top-down approaches like peeling, sonication, ball milling, and exfoliation and bottom-up methods include chemical vapor deposition, silicon evaporation, epitaxial growth, using an electric arc etc. But these procedures are less capable of producing enough amount of defect less pristine graphene at a low cost and at a large scale due to poor solubility and agglomeration. As a consequence, for experimental purposes, researchers made extensive utilization of graphene oxide (GO) which has similar properties to pristine graphene prepared by oxidizing graphene by oxidizing agents. GO is mostly a single monomolecular layer of graphite covalently functionalized with oxygen-containing groups (carboxyl, epoxy, and hydroxyl) on the basal plane and sideways of the structure. Unlike graphene, GO can be produced in vast quantities at a reasonable cost by using a simple processing approach. Furthermore, GO has excellent water dispersibility as its

hydrophilic by nature and consists of both aromatic (sp^2) and aliphatic (sp^3) regions which results in easy surface interaction with a variety of different molecules. Because of other prominent properties of GO like optical, electrical and mechanical abilities, it is used as an active material in many synthesized composite materials and also as precursor for a plethora of applications including photocatalysis, bioimaging, solar cells, lithium-ion batteries (as electrode material), supercapacitors, fuel cells, medicine, biosensing, drug delivery, water purification and many more.

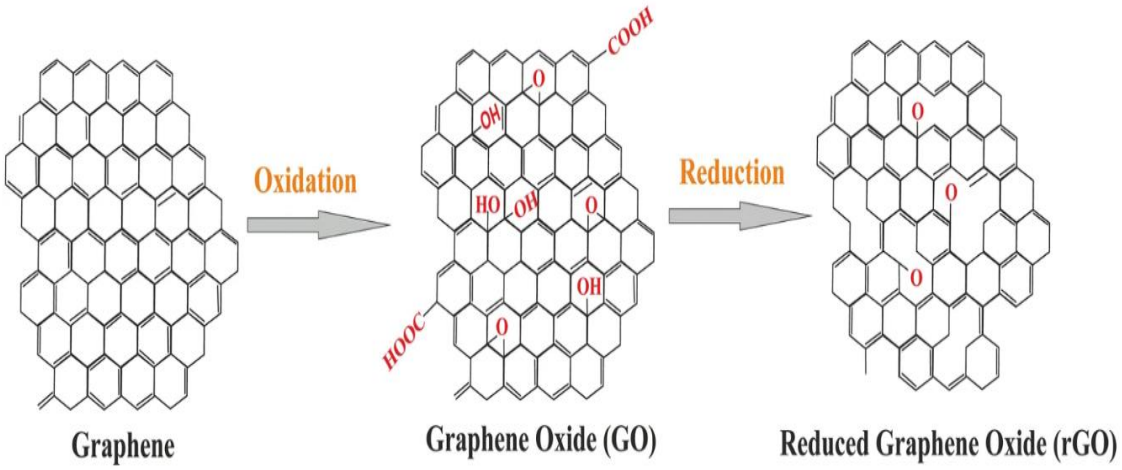

Figure 5: Conversion of graphene into GO and rGO [62].

GO can be quickly generated from graphite flakes using widely recognized chemical and electrochemical exfoliation procedures based on techniques proposed by Hummers, Staudenmaier, Offeman, Brodie or different modern methods proposed by other researchers [66]. We have opted for the modified Hummers method in our experiment for producing GO. The usage of strong oxidizing agents like potassium permanganate can disturb the crystalline sp^2-bonding network of GO to some extent which impacts its electrical conductivity instigating semi-conductive or insulative behavior. But the chemically reduced state of GO which is denoted as rGO (reduced graphene oxide) possesses a similar level of conductive properties of pristine graphene because of the presence of π network and fractional recombination of carbon−carbon double bonds, see the structures in Figure 5. The large surface area of rGO provides a potentially high density of surface active sites that is beneficial for the high capacity energy storage devices and various catalytic reactions like H_2 evolution reaction, CO_2 reduction reaction, N_2 reduction reaction, and O_2 reduction reaction.

rGO can be easily and economically produced in bulk quantities by eliminating the oxygen functional groups from graphene oxide following several reduction procedures like thermal

reduction, microwave-assisted reduction, photo chemical reduction, chemical reduction, electrochemical, ultraviolet radiation or solar mediated reduction procedures by applying different reducing agents. The properties and quality of rGO depend on the degree of reduction as well as on the conducted reduction methods. In our work we have followed the thermal reduction technique to produce rGO at an oxygen free environment and optimal temperature. The thermal reduction methods is more environment friendly and give higher reduction degree than chemical reduction methods [63], [64], [65] .

rGO has also been proved as an excellent support material in combination with different kinds of electroactive materials for the CO_2RR. Takuya Tsujiguchi et al. studied the effects of rGO for a synthesized composite catalyst Sn/rGO for Electrochemical CO_2 reduction to formate. They analyzed through the Density functional theory (DFT) calculations that the synergistic effect of rGO as catalyst support increased the CO_2 absorption rate 8.1-times faster and absorption capability 4 times more than only single atom tin (Sn) nano catalyst. This is due to the availability of oxidized functionalized CO_2 absorption sites of rGO on the composite catalyst surface. They also observed that CO_2 reduction ability of Sn/rGO800 was higher than Sn/G800, Sn particles, and rGO.The Faradic Efficiency was also enhanced 1.8 times over +90% due to rGO catalyst support [66].

Hui-Yun Jeong and team used tris(2-benzimidazolylmethyl)amine (NTB) ligand as linker to uniformly dispersed single-atom nickel ion over N-doped rGO sheets. This NTB ligand worked as a binder between Ni ions and the GO sheets and formed a stabilized Ni(NTB)-GO complex through π-π interaction with GO sheet and ligation with transitional metal Ni ion. By annealing the complex at high temperature (800°C) and at inert (Ar) condition, thermally reduced Ni-N-rGO complex catalyst was produced and employed for electrochemical reduction of CO_2 reaction to CO. They compared the catalytic activity of Ni-N-C and Ni-N-rGO complex and observed a higher catalytic activity of Ni-N-rGO than that of Ni-N-C complex, showing a more positive onset potential of −0.6 V vs RHE at the current density of −5 mA/cm^2 under CO_2. FE for CO product is 70% at −0.4 V vs RHE near the onset potential. The FE also increased as the applied potential amplified and reached its maximum of 97% at −0.8 V vs RHE (reversible hydrogen electrode). At −1.0 V vs RHE, high current density of −42 mA/cm^2 is also detected. This indicated that the high surface area of rGO sheet has not only facilitate the synthesis of a stable nanoparticle single atom electrocatalyst but also improved its overall catalytic performance for CO2 electroreduction [67].

1.4 CO_2 ELECTROREDUCTION:

CO_2 electroreduction is a promising approach of applying electrical energy or non/low carbon energy sources to convert captured CO_2 into reduced and functional chemical commodities and fuels to manage the global carbon cycle and lessen the dependence on fossil fuels. The CO_2 reduction electrolyzer basically consist of a cathode that is responsible for CO_2 reduction, whereas the anode is responsible for oxygen oxidation (from water).

CO_2 is a thermodynamically stable molecule because of which the dissociation of the O=C=O bond needs a high activation energy.To break C=O bond requires to overcome a high-energy barriers of about 750 kJ/mol which leads the overall CO_2 ERR to low energy efficiency. Moreover, the applied potential for the first direct one electron CO_2 reduction to get $CO_2^{\cdot-}$ radical anion is - 1.9 V vs SHE (standard hydrogen electrode), which is highly negative redox potential and makes the overall reaction kinetics slow. The poor solubility of CO_2 in the most frequently used aqueous electrolyte solution also slows down the CO_2RR reaction activity. During CO_2 reduction a simultaneous Hydrogen evolution reactions (HER) occurs at cathode as a side reaction of hydrolysis of water which also act as proton donors for the CO_2 RR. The redox potential range of many end products and HER thermodynamic on set potential are similar which leads to poor selectivity of a particular desired final product.

A significant number of studies have revealed that the production of the reduced end compounds are dependent on several factors such as electrolyte, highly functioned electrolyzer, electrocatalyst properties, the reactions working conditions like proton obtainability, applied cathode voltage, carbon dioxide concentration, mass transport, pH, and temperature. In most of the conducted experiments, the catalyst lifetime was under 100 h.The electrode's surface structure also has a substantial impact on the catalytic performance of CO_2RR. Therefore, a stable electrocatalyst is inevitable for CO_2 electro reduction to minimize this overpotential need, increasing the current densitiy, improving the energy efficiency and selectively deliver the desired hydrocarbons without being interrupted by any undesired side-reactions and at a industrial level [68], [69], [70].

These electrocatalysts have been classified into homogenous and heterogenous catalysts. Homogenous catalysts are basically organic compounds or organometallic materials (enzymes and molecular catalysts) with low overpotential, functional structure, great selectivity and

suitable kinetics for CO_2 reduction but because of their low thermal stability, poor electrolyte solubility, high cost, non-recyclability and difficulty in product separation, its practical and scalable application has becomes limited as electrocatalyst for CO_2 RR. To overcome these downsides, researchers are lately more interested in employing heterogeneous electrocatalysts for effective CO_2RR [71].

The electrocatalysis process of CO_2 follows a several numbers of reaction pathways to produce different compounds. CO_2 Electroreduction is a multistep complicated process that involves the transfer of multiple protons and electrons that can be denoted as CPET (couple proton electron transfer process including 2e, 4e, 6e, 8e, 12e or 18e at different applied potentials at the electrodes, while also yielding diverse reduction compounds. For instance, formic acid (CO_2 + 2e- + 2H→ HCOOH) and carbon monoxide CO (CO_2 + 2 e- + 2H→ CO + H_2O) will be produced during two electron reduction pathway.

In the case of multiple electron transfers, more complex hydrocarbons can be achieved like: Methanal (CO_2 +4e- + 3H_2O → HCHO + 4OH-), methanol (CO_2 + 6e- + 6H→ CH_3OH + H_2O), methane (CO_2 + 8e- + 8H→ CH_4 + 2H_2O), ethanol (2 CO_2 +12e- + 12H→ CH_3CH_2OH + 3 H_2O), propanol (3 CO_2 + 18e- + 18H→ C_3H_7OH +5H_2O).

Generally, the overall electrochemical reduction reaction of CO_2 happens at the interface of the electrocatalyst on the electrode surface and the electrolyte solution. This whole process consists of three main steps that are: (1) the adsorption of CO_2 on the electrocatalyst surface 2) CO_2 will then be reduced to an intermediate form such as $*CO_2^{\cdot-}$ or *COOH through electron/proton transfer process across the interface. 3) finally the produced compound migrate into the bulk electrolyte solution.

The production of final products usually depend on the bond formed between the activated $CO_2^{\cdot-}$ radical and catalyst, an example shown in Figure 6. During the adsorption step if the O atom of activated $CO_2^{\cdot-}$ connects to the catalytic site then HCOO will form in the intermediate step which will finally form formic acid after further protonation. But if C atom of $CO_2^{\cdot-}$ binds to the catalytic site, *HOCO and then CO will be formed as intermediates. If CO adheres to the surface poorly, the intermediate will release and eventually create CO. If *CO bindes strongly, then the intermediate step will go through a more intricate process involving more e-transfer and protonation, resulting in the creation of various hydrocarbons or alcohols [13], [15].

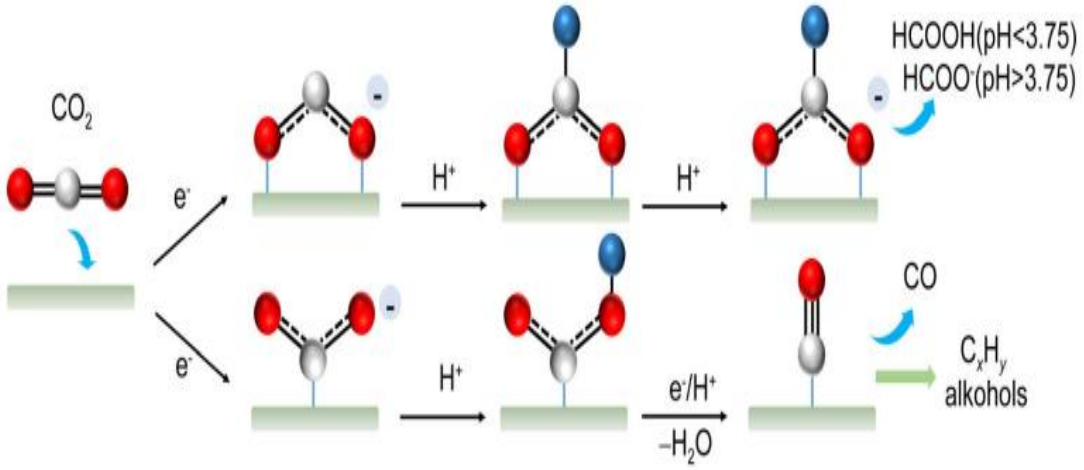

Figure 6: Possible reaction pathways for electrochemical CO_2RR to formate, CO, and other products [13].

It has been observed in many studies conducted so far that the faradic efficiency (FE ~ 100%) for producing C1 products (CO, CH_4, $HCOO^-$, and CH_3OH) from CO_2 electroreduction is higher with a less complex reaction pathways compare to the C2 product (C_2H_4) (FE ~60%) and C3 product (n-C_3H_7OH) (FE <10%). This is because of a complex and unsettled reaction mechanism and higher energy requirement, which limits the practical utilization of CO_2 transition to C2 and C3 products in commercial electrolyzers [72].

In 1980, Hori group first tested a number of pure metal electrodes catalyst for CO2RR and classified them into 3 main groups. (1) Transition metals like Ag, Au, Pd that produce CO as their primary product. (2) Metals like Sn, Pd, Bi, that produce HCOOH as their main byproduct. (3) Cu was the only metal that can produce a sizeable amount of hydrocarbons and multi-carbon compounds [73]. Metal electrodes have been investigated and applied for many years as a potential electrocatalyst for effective CO2ERR but due to their relatively low active surface space various other catalyst like single atom catalyst (Fe,Cu,Zn), bimetallic catalyst (CuIn,PdPt), molecular catalyst ($Re(bpy)(Co)_3$, noble metal catalysts (Au, Ag, Pd), nanostructured (nanoparticles, nanoclusters, nanowires) electrocatalysts have gained the attention of the researchers for CO_2ECR over the years. Their improved surface area has boosted the CO_2 reduction activity, selectivity and high current density [74].

Jonathan Rosen et al. investigated a nanostructured Ag electrocatalyst included both nanoparticle and nanoporous in an aqueous electrolyte for CO_2 reduction. The large Ag surface area and increased surface site activity reduce the activation energy of the intermediate CO_2 to

$COOH_{adp}$ step, leading to a reaction mechanism with a fast first electron and proton transfer followed by a slow second proton transfer as the rate-limiting step [75].

Kristian Torbensen et al. studied a molecular electrocatalyst, Co phthalocyanine (CoPc2), a phthalocyanine macrocycle consist of three tert-butyl groups attached to it and one trimethyl ammonium moiety immobilized on an electrode. This Cobalt complex demonstrated same electronic and steric properties for CO_2 ECR to CO in water solution with high selectivity (ca. 95%), maximum current density of 165 mA cm^{-2} (at −0.92 V vs. RHE) and good reaction stability over an extended period of time of 10h experiment [76] .

Anna Klinkova and her colleagues employed a traditional and noble metal catalyst Palladium (Pd) nanostructured form to improve its catalytic performance and stability for CO_2 reduction to liquid formate fuel. They observed the surface of Pd catalyst and saw a low overpotential of -0.2V with a high current density of 22mA/cm^2 and FE of 97% which could be attributed to the controlled morphology of Pd surface [2], [77], [78].

A bimetallic Cu-Sn electrode was generated by S. Sarfaraz et al. by electrodepositing Sn particles onto the oxide-derived copper (OD-Cu) surface. A Cu-Sn catalyst surface with reduced H_2 adsorption and good selectivity, as well as FE >90%, were demonstrated by DFT calculation for CO generation from CO_2 over a broad potential range (−0.4 to −0.8 V vs RHE) [78] .

Recently, MOF-based electrocatalysts have also demonstrated excellent performance in CO_2 reduction because they combine the benefits of homogeneous and heterogeneous catalysts. Using a cobalt−porphyrin MOF, $Al_2(OH)_2$TCPP-Co (TCPP-H_2= 4,4′,4″,4‴-(porphyrin-5,10,15,20-tetrayl)tetrabenzoate) based electrocatalyst, Nikolay Kornienko et al. were able to improve catalytic performance overall and obtain high selective CO yielding 1400 turnover number (TONNE) and 76% Faradaic efficiency [79] .

2 EXPERIMENTAL PART

2.1 Materials and Methods:

Chemicals and reagents: TiO_2 (P25) (Rutile:anatase:85:15), crystal size 20 nm was purchased commercially. Graphite, 5,10,15,20-tetrakis(4-aminophenyl)porphyrin, Meso tetra (4-amino phenyl) Zinc porphyrin, Meso tetra (4-amino phenyl) Nickel porphyrin were bought from commercial supplier Por-Lab.

$TBPAF_6$, DMF, Diethyl ether, KCl were purchased from Sigma-Aldrich and used as received. THF was purchased from Riedel-de Haen.DI (Deionized) water and ethanol (99.5%) were used for synthesis purposes. All reagents and solvents were analytical grade and used as received without further purification.

A teflon lined autoclave (see Figure 7) was used for samples synthesis purpose.

Figure 7: The used Teflon lined autoclave

2.2 Synthesis of GO by modified Hummers method:

The production of graphene oxide was carried out by following the modifying Hummers' method reported by Hiratan et al. [80]. First, 2.0 g of powdered graphite and 1.5 g of sodium nitrate ($NaNO_3$) were amalgamated with 124.2 g of sulfuric acid (H_2SO_4)(67.5 ml) in a 3 neck bottle placed in an ice bath. 9 g of $KMnO_4$ was added gradually for a period of 30 minutes into the mixture and the mixture was kept for two hours to react in the ice bath. The solution was left for 5 days to react well while maintaining the mixture temperature equivalent to room temperature by using a water bath of the melted ice. The solution color changed from black - greenish to brownish. To finished the oxidation process 200 ml of 5 w-% sulfuric acid was added drop wise into the graphene oxide mixture in an ice bath and stirred for one hour in the room temperature. This results in a dark brown solution. Finally, 6 ml of 30% H_2O_2 solution was dropped into the reaction mixture, which turned the color of the solution into light brown, confirming GO formation and stirred for two hours.

To achieve neutral pH and removed the excess H_2SO_4, the formed GO is then repeatedly washed and centrifuged and the precipitate redispersed into clean water in large glass centrifugal tubes. Next, diluted graphene oxide is placed into a dialysis tube for dialysis and the tube is placed in water bath. After 15-20 dialysis, when the absorbance spectra of the outer solution shows no signs of significant absorbance the dialysis was finished and GO was collected from the dialysis tube.

2.3 Synthesis of rGO-TiO_2 nanocomposite:

rGO-TiO_2 nanocomposite was synthesized by following a customized hydrothermal method. At the beginning of the synthesis process of rGO-TiO_2, the bulk GO, prepared by modified Hummer's method was sonicated for 10 minutes before using it.7ml of GO (5mg /ml) and 39 ml of DI water were added and sonicated for 1 hour for proper dispersion by maintaining the temperature below 32°C. Next, in the same mixture, 35 mg of P25 powder and 23.3 ml EtOH (99.5%) were further added and stirred for 2 hours at a constant medium speed with a magnetic bar at room temperature to ensure a homogeneous solution. The theoretical ratio maintained of EtOH: H_2O=1:2.The total 70 ml of brownish-coloured solution was then transferred into a Teflon liner and the sealed Teflon lined flask was put inside a stainless steel autoclave which

was then placed inside a vacuum oven at 150℃ for 18h . The autoclave was gradually cooled down to room temperature. The obtained solution was centrifuged at 8500 rpm for 20 minutes each time and washed with DI water several times until the filtrate was clear. Before each round of centrifugation, the sample was sonicated for 5 minutes to avoid agglomeration. Lastly, the gained sample was dried overnight at 30℃ in the air inside a vacuum oven. After drying approximately 35 mg of composite sample was retrieved.

2.4 TiO_2 treatment:

Commercial TiO_2 (P25) powder was hydrothermally treated for background checking 30 mg of P25 powder was added into 20 ml of DI water with 10ml of EtOH (99.5%) to prepared a 30ml of total solution (H_2O:EtOH::1:2). The solution was stirred for 2 h and then poured into a Teflon lined autoclave which was heated to 150℃ for 18 h inside a vacuum oven. The autoclave was left to cool down to room temperature .The sample was then centrifuged at 8500 rpm for 10 minutes and washed three times with DI water. Finally, the sample was dried in a petri dish overnight at 30℃ inside an oven.

2.5 Synthesis of Reduced Graphene oxide:

To prepared reduced graphene oxide (rGO) a measured amount of GO (6 ml) was taken from bulk GO (5 mg/ml) after 10 minutes of sonication. GOwas mixed with 14 ml of DI water followed by ultrasonication for 1 h and vigorous stirring for 2 h. The autoclaved liner filled up by the mentioned solution was placed inside a vacuum over for 18 h at elevated temperature of 150 ℃ for GO reduction. After cooling the solution was centrifuged (at 8500 rpm,20 minutes) and washed with DI water few times until the filtrate looks clear. The washed sample was dried in a petri dish overnight at 30℃.

2.6 Synthesis of rGO-TiO_2 /TAPP, rGO-TiO_2 /Ni-TAPP and rGO-TiO_2 /Zn-TAPP nanocomposites:

By following the standard procedure 100 mg of rGO-TiO_2 composite powder was dissolved into 15 ml of DMF solvent. Subsequently, 5 mg of TAPP was added to the solution and stirred for half an hour for uniform dispersion. A 30 ml Teflon lined autoclave filled with the mentioned solution was heated at 120 ℃ for 6 h in a vacuum oven. The cooled solution was centrifuged initially with diethyl ether and then two times with THF for 5 minutes each time at 3500 rpm to remove the unbound TAPP. Afterwards, the sample was further washed with DI water two times for 10 minutes at 8500 rpm to get rid of all the impurities. The sample was dried inside a vacuum oven for 7 h at 60℃ temperature.

The same above-mentioned procedure was followed for preparing rGO-TiO_2 /Ni-TAPP and rGO-TiO_2 /Zn-TAPP nanocomposites but instead of TAPP, metal porphyrins Ni-TAPP and Zn-TAPP were added respectively.

2.7 Preparation of Catalyst ink on Glassy Carbon electrode :

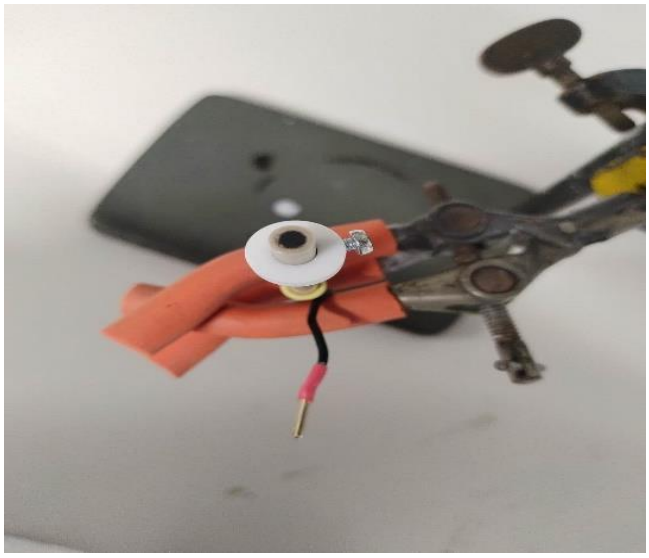

Figure 8: Glassy carbon electrode surface with drop casted catalyst ink.

Catalyst ink was prepared for drop casting it on a glassy carbon electrode (GCE) surface for electro-reduction of CO_2, see Figure 8.Catalyst ink different samples (TiO_2,GO,rGO, rGO-TiO_2 composite, rGO-TiO_2 /TAPP, rGO-TiO_2 /Zn-TAPP and rGO-TiO_2 /Ni-TAPP) was prepared by dispersing 1 mg of the sample in 1 ml of ethanol (99.5%). Ultrasonic treatment was used for 20 minutes to break down the composite flakes into small particles and for homogenous

dispersal into the solvent. Total 30 µl (3 µl each time, 10 times) catalyst ink was drop cast on the surface of a glassy carbon electrode (GCE) and the surface was dried with a top gun The surface of the GCE was coated with the thin catalyst film after completing each drop casting process.

3 CHARACTERIZATION

3.1 Fourier-transform infrared spectroscopy (FT-IR):

In this experiment, FTIR analysis was performed to identify the synthesized compounds by detecting their functional groups by absorbing the infrared radiation.
All the nanocomposite samples were characterized by Bruker Vertex 70 FTIR spectrometer with an MCT detector cooled with liquid nitrogen with attenuated total reflectance (ATR-IR) plate-smart orbit crystal with 120 scans, resolution 4 cm^{-1}.

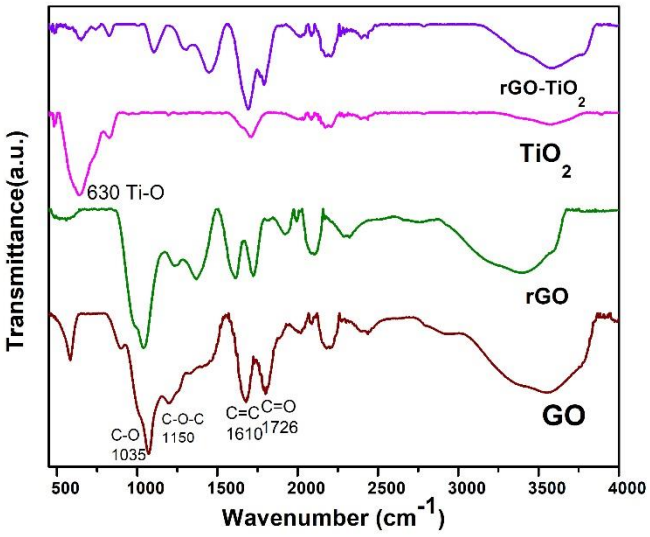

Figure 9: FTIR spectra of GO, rGO, TiO_2 and rGO-TiO_2 materials

FTIR spectra of the compounds are shown in Figure 9.The FTIR spectra of GO demonstrated signals for C-O, C=C, C=O and OH functional groups which confirm the the presence of carbonyl, epoxy, carboxyl and hydroxyl groups. The peaks that appeared at around 1035 cm^{-1} were responsible for the C-O alkoxy groups stretching vibration band and 1150 cm^{-1} (C-O-C) was attributed for epoxy. The band stretching at 1610cm^{-1} was for the presence of aromatic sp2 C=C functional group. The presence of carbonyl C=O functional groups were observed at 1726 cm^{-1} band stretching [81], [82], [83].The broad signal between 3100 cm^{-1} to 3700 cm^{-1}

was corresponding to hydroxyl (OH) functional groups of GO specifically the wide peak at 3406cm^{-1}[83], [84] .

The peak intensity and position for rGO has notably altered which was clearly visible in the FTIR signals for rGO. This indicates the partial reduction of GO. The intense peak at 630cm-1in the lower FTIR spectra region of TiO_2 was appeared because of Ti-O stretching vibration band [84].

The Corresponding signals of rGO-TiO_2 nanocomposite's FTIR spectra were in accordance with most of GO, rGO and TiO_2 FTIR spectrums indicating rGO-TiO_2 composite has been successfully synthesized. Low frequency bands presence around 670 cm^{-1} indicates the vibration stretching of Ti-O-C due to the bond formation between rGO and TiO_2 [82].The Ti-O peak intensity is observed at TiO_2. The absorbance in the FTIR spectra were comparatively lower in rGO-TiO_2 spectra which confirms that TiO_2 has been covered with rGO in the prepared composite sample.

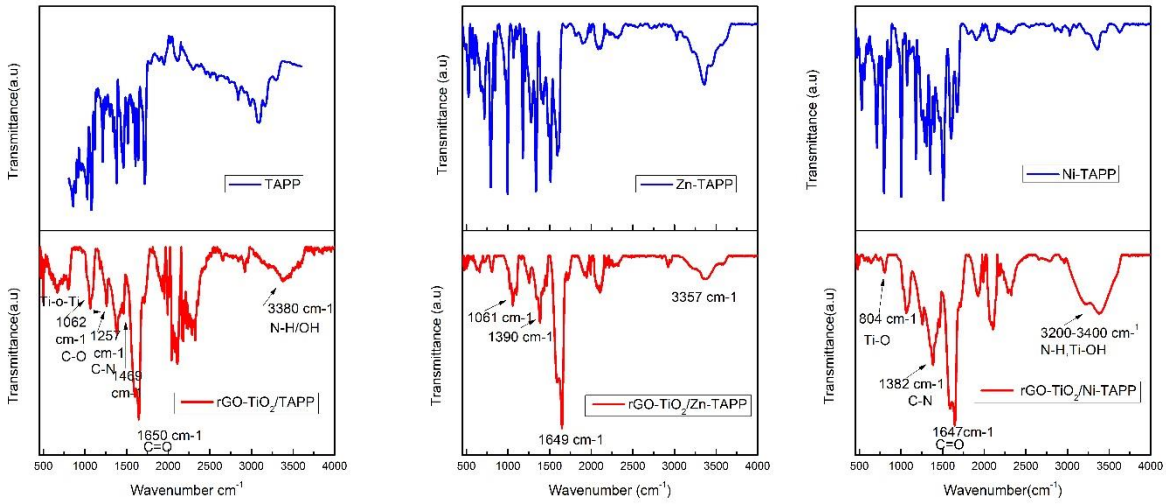

A) B) C)

Figure 10: FTIR spectra of A) rGO-TiO_2 / TAPP , B) rGO-TiO_2 / Zn-TAPP and C) rGO-TiO_2 /Ni- TAPP composites respectively.

The formation of rGO-TiO_2/TAPP, rGO-TiO_2 / Zn-TAPP and rGO-TiO_2 /Ni-TAPP nanocomposites and their chemical structure were confirmed by studying their respective FTIR spectrums. In the Figure 10, the lower intensity of the absorption bands that appeares approximately between 500 cm^{-1} to 800 cm^{-1} range in all of the three composites spectra were due to the vibration of Ti-O-Ti bonds, which also was observed in TiO_2 and rGO-TiO_2 FTIR

spectra [85]. This confirms the bond creation between the rGO-TiO_2 and the three metal porphyrin complexes.

In Figure 10 showing FTIR spectra, the peak intensities and positions of the three rGO-TiO_2 /metal pophyrin nanocomposites have drastically changed. The oxygen containing C=O groups from GO around 1726 cm^{-1} was weakly visible in the FTIR spectra of the hybrid nanocomposites [82]. A strong new vibration band at around 1650 cm^{-1} and a stretching band at 1257 cm^{-1} observed in all the three hybrid rGO-TiO_2 /Porphyrin compounds which is characteristic forC=O stretching of primary amide and stretching band of C−N respectively. Bands appeared around 1062 cm^{-1} (C-O stretching vibration), around 1469 cm^{-1} (amine -NH bending) and around 1386 cm^{-1} (C-N stretching) confirmed that -NH_2 group of TAPP and the two metalloporphyrin complexes bonded with the COOH functional groups of GO, forming C-N covalent bonds through amide linkage [81]. The peaks around 3380cm^{-1} can be attributed to the stretching vibrations of N-H and surface hydroxyl groups (OH) of TiO_2 (Ti-OH) [85].
The presence of amine N-H and C-N characteristics band in rGO-TiO_2 / TAPP, rGO-TiO_2 / Zn-TAPP and rGO-TiO_2 /Ni-TAPP nanocomposites indicates the successful hybridization of rGO-$TiO_2$with TAPP and two metalloporphyrin complexes to form the hybrid nanocomposites.

3.2 Raman Spectroscopy analysis:

The samples chemical structural changes and molecular interactions were examined by using Raman spectroscopy. The Renishaw Qontor in Via Raman microscope instrument was used with 532 nm excitation laser power for all measurements of the prepared nanocomposites. The nanocomposite sample was drop casted on a sample holding slide. Raman spectra of the compounds are shown in Figure 11.

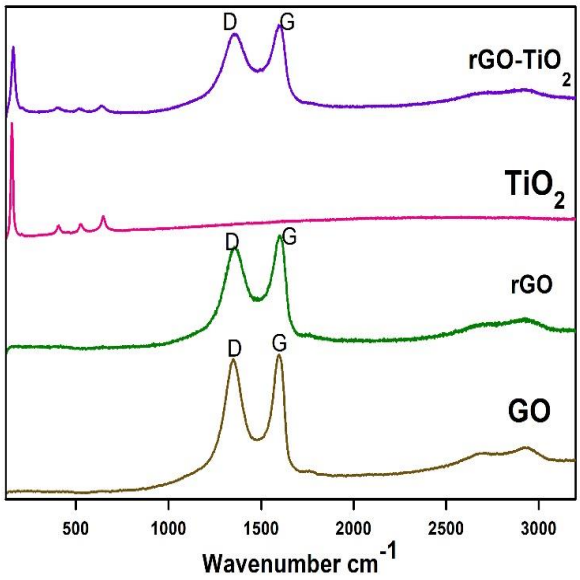

Figure 11 : Raman spectra of GO,rGO,TiO_2 and rGO-TiO_2 samples.

Two strong peaks were observed stated as D which is stretching at around 1350 cm^{-1} and the adjacent peak G located at around 1596 cm^{-1} band stretching in GO ,rGO and rGO-TiO_2 Raman spectrum. This two D and G bands are the main GO characteristic peaks. In case of GO, D and G bands peak intensity implies disruption of graphitic hexagonal lattice due to oxygen containing groups. The D band mostly is a representation of structural flaws, vibration of sp^3, edge effects and dangling of sp^2 carbon atoms that cause the hexagonal graphitic lattice to dislocate and break symmetry. G is ascribed to the in-plane vibrational stretching motion between sp^2 carbon atom [86].

The high intensity peak at 145 cm^{-1} in TiO_2 Raman spectra corresponds to the symmetrical stretching mode of Ti-O bond. The low Raman bands observed at 397 cm^{-1} ,513 cm^{-1} and 643 cm^{-1} can be assigned to the anatase phase of P25 [82] .

In rGO-TiO_2 Raman spectrum it can be observed that a number of typical TiO_2 and rGO related Raman bands has appeared.The band intensity of TiO_2 in rGO-TiO_2 was also considerably decreased with increased amount of GO content in the sample. This confirms the successful loading of TiO_2 on the GO surface.

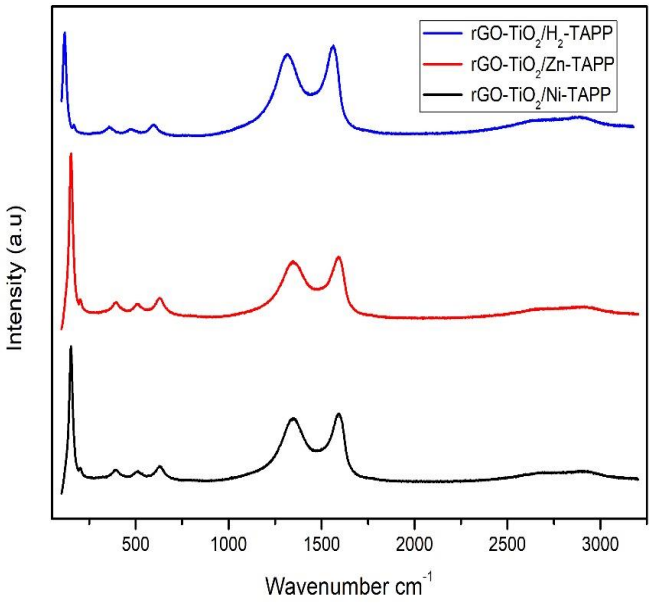

Figure 12:Raman spectra of rGO-TiO_2 / H_2-TAPP , rGO-TiO_2 / Zn-TAPP and rGO-TiO_2 /Ni-TAPP samples.

In case of synthesizing the hybrid nanocomposite of the porphyrin metal complexes the amount of the used H_2-TAPP, Zn-TAPP and Ni-TAPP were so low that in the Raman spectrum of the all the three rGO-TiO_2 / H_2-TAPP , rGO-TiO_2 / Zn-TAPP and rGO-TiO_2 /Ni- TAPP nanocomposites no detectable Raman signal was observed for the porphyrin complexes, Figure 12. But the Raman peaks for rGO and TiO_2 were clearly visible.

3.3 Powder X-ray diffraction :

PXRD was conducted to verify the formation of the composite materials through identifying their crystalline phase.

The XRD pattern of TiO_2 nanoparticles in Figure 13 showing the blended crystal phase of anatase (marked with A) and rutile (marked with R) with certain number of diffraction peaks at 2θ angle . The 2θ= 25.28˚, 37.83˚, 47.86 ˚, 53.843˚ and 54.841˚ with diffraction planes (101), (004), (200), (105) and (211) respectively are responsible for anatase phase , while 2θ= 27.38˚

and 36.07 ˚ are corresponds to 110 and 101 rutile crystal plans (JCPDS No. 01-075-2547 and 01-JCPDS No. 079-6031) [87].

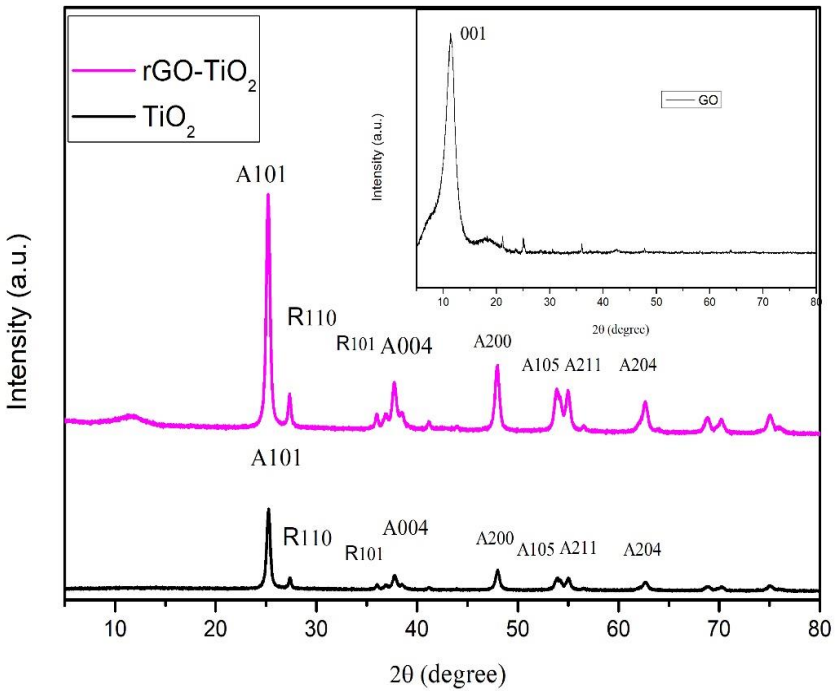

Figure 13: PXRD spectrums of GO, TiO_2 and rGO-TiO_2

In the XRD spectrum of the composite rGO-TiO_2 we can observe a wide characteristic peak at 2θ = 11.65 ˚ which is attributed to the GO plane that can be also seen in the inset figure of GO XRD spectrum at 2θ = 11.46 ˚ with a sharp high diffraction peak (001). In addition, other characteristic crystal diffraction peaks of TiO_2 were also seen in the similar spectrum. Moreover, the partial disappearance and the broadness of the GO peak (001) in the rGO-TiO_2 composite indicates the successful reduction of GO to rGO. Additionally, the shift of GO peak from 11.46 ˚ to 11.65 ˚ in the rGO-TiO_2 composite because of the bond formed between the surface carbon groups of rGO and TiO_2 to synthesize rGO-TiO_2 nanocomposite [82].

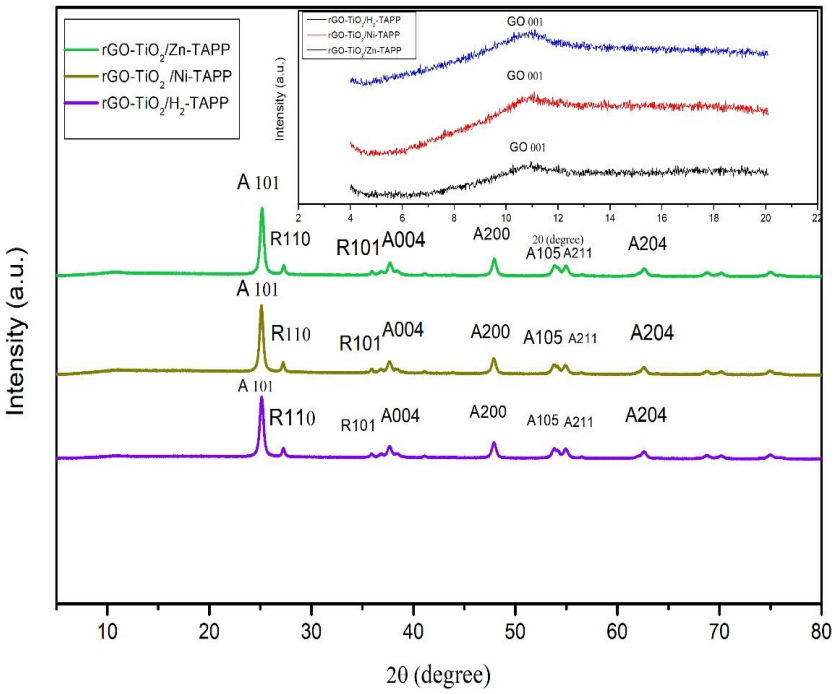

Figure 14: PXRD patterns of rGO-TiO_2/TAPP, rGO-TiO_2 /Ni-TAPP and rGO-TiO_2 /Zn-TAPP .

The similar diffraction peaks of the rGO-TiO_2 nanocomposite have been observed in the XRD spectrums of the three nano hybrid composites denoted as rGO-TiO_2/TAPP, rGO-TiO_2 /Ni-TAPP and rGO-TiO_2 /Zn-TAPP. No visible change in the standard peaks of the rGO-TiO_2 (Figure 14) was observed during loading of TAPP, Ni-TAPP and Zn-TAPP on the rGO-TiO_2 composite. It could be due to the small amount of TAPP and metal porphyrin complexes and their weak crystallinity [88]. This also implies that the hybridization of rGO-TiO_2/TAPP, rGO-TiO_2 /Ni-TAPP and rGO-TiO_2 /Zn-TAPP with rGO-TiO_2 has slight effect on the crystal form of TiO_2 [82]. From the inset in Figure 14 of GO of the composite materials it can be observed that the diffraction peak 001 has been slightly shifted to $2\theta = 11.04^{\circ}$ (black line), 11.05° (red line) and 10.88° (blue line) respectively from $2\theta = 11.65^{\circ}$ (rGO-TiO_2) and broadened which could be attributed to the change in the lattice parameter because of GO reduction to rGO and the sensitization of rGO-TiO_2 with TAPP, Ni-TAPP and Zn-TAPP compounds.

3.4 X-ray photoelectron spectroscopy measurements:

XPS analysis was conducted to study the nature of the connection between the complex materials along to get their surface chemical state information. The XPS results are shown in Figure 15.

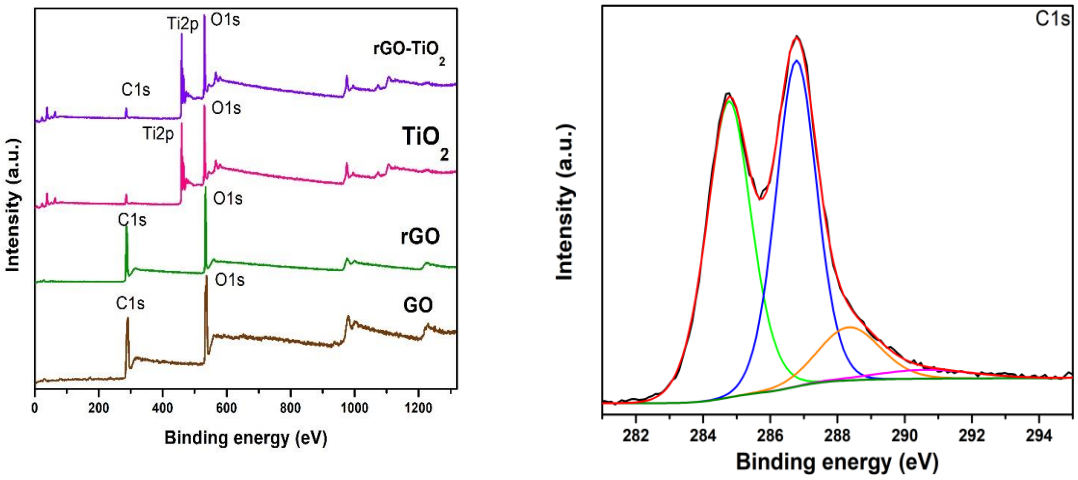

A) B)

Figure 15 : XPS results of A) GO, rGO, TiO_2 and rGO-TiO_2 full survey scan spectra B) for C1s of rGO-TiO_2.

Two peaks seen at 292 eV and 538 eV in the full scan survey of GO (Figure 15) were corresponding to C and O respectively. In rGO, the C and O related peaks slightly blue shifted at 285 eV and 533 eV respectively which can be owing to the reduction of GO.

Peaks related to both GO and TiO2 were observed in the full scan survey of rGO-TiO_2. The less intensity of C in rGO-TiO_2 composite's XPS is due to the loading of TiO_2 on graphene sheet. The intense peak centered at 459 eV in rGO-TiO_2 XPS indicates the presence of Ti in the formed composite [82].

The high resolution deconvoluted spectrum and the peak of C1s of rGO-TiO_2 composite showed C-C and C=C bonds binding energy at 284.78 eV. (Moreover, other deconvoluted peaks represented a C-O-Ti bond peak at 286.88 eV and C-O bond peak at 288.38 eV binding energy originated from the rGO-TiO_2 composite [89] .These peaks are strong prove for that rGO-TiO_2 has successfully synthesized.

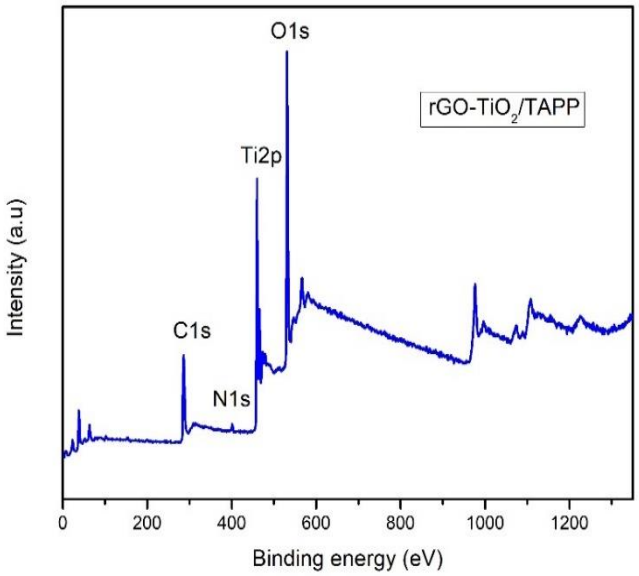

Figure 16: The full survey XPS spectrum of rGO-TiO_2/TAPP.

The XPS survey spectrum of rGO-TiO_2/TAPP in Figure 16 reveals that the rGO-TiO_2/TAPP composite is composed of C, Ti, O and N components. The presence of less intense N1s peak BE at 401,42 eV indicates that TAPP porphyrin complex has formed a bond with the surface of rGO or TiO_2 to synthesized rGO-TiO_2/TAPP material.

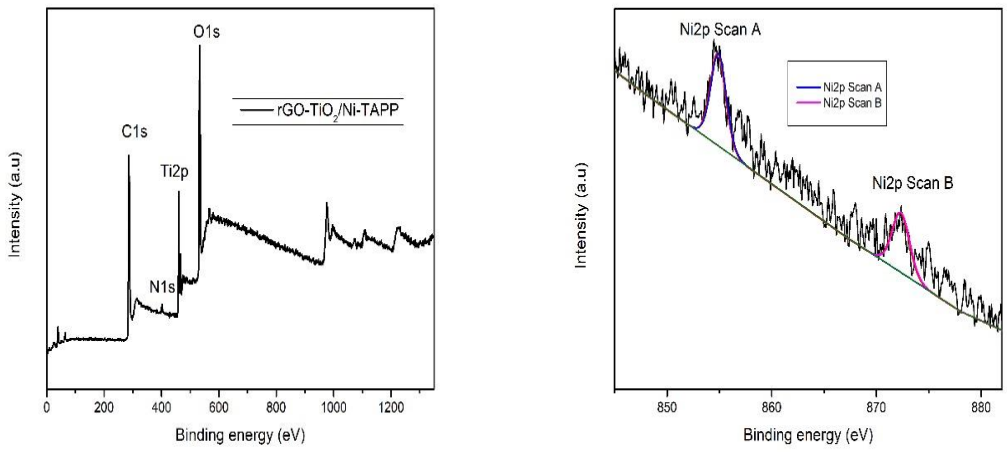

A) B)

Figure 17: XPS spectra of A) rGO-TiO_2/Ni-TAPP full survey B) Ni 2p region

The XPS spectra of rGO-TiO_2/Ni-TAPP clearly suggesting the existence of C1s, N1s, Ti2p and O1s materials in the rGO-TiO_2/Ni-TAPP sample. The presence of the Ni metal in the metalloporphyrin complex contained rGO-TiO_2/Ni-TAPP composite has been identified by the signals of Ni 2p (Figure 17) which can be deconvoluted into two peaks for Ni 2p3/2 (scan A) at 854,83 eV and Ni2p1/2 (Scan B) located at 872,27 eV.

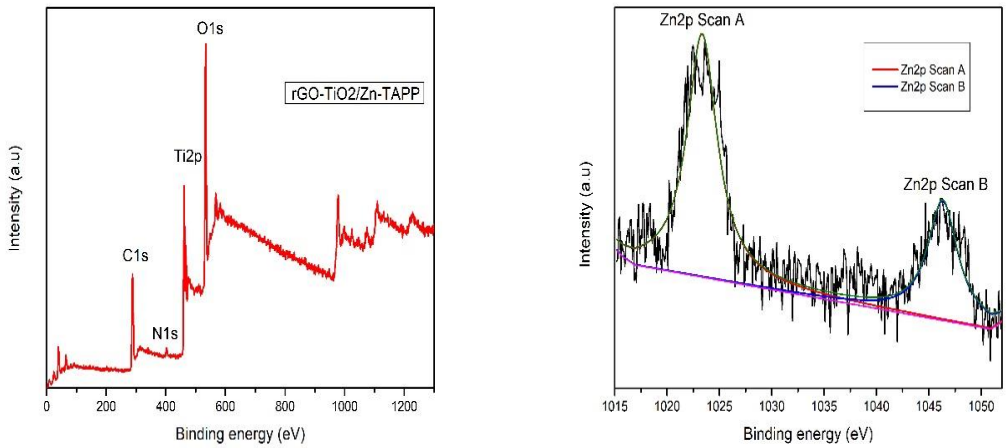

A) B)

Figure 18: XPS spectra of A) rGO-TiO_2/Zn-TAPP full survey B) Zn 2p region

In the case of rGO-TiO_2/Zn-TAPP, the full XPS survey spectrum (Figure 18) confirms the C, Ti, O and N composite materials same as the other two porphyrin contained hybrid samples. In Figure 18, high-resolution Zn 2p spectrum with two BE peaks that can be referable to both Zn 2p3/2 at 1023,34 eV and Zn 2p1/2 at 1046,32 eV confirms the presence of Zn metal in the rGO-TiO_2/Zn-TAPP composite [90].

3.5 Thermogravimetric analysis:

TGA was performed under N_2 to observe the thermal degradation of the synthesized samples at a specific temperature 1400℃ and weight (~10mg).

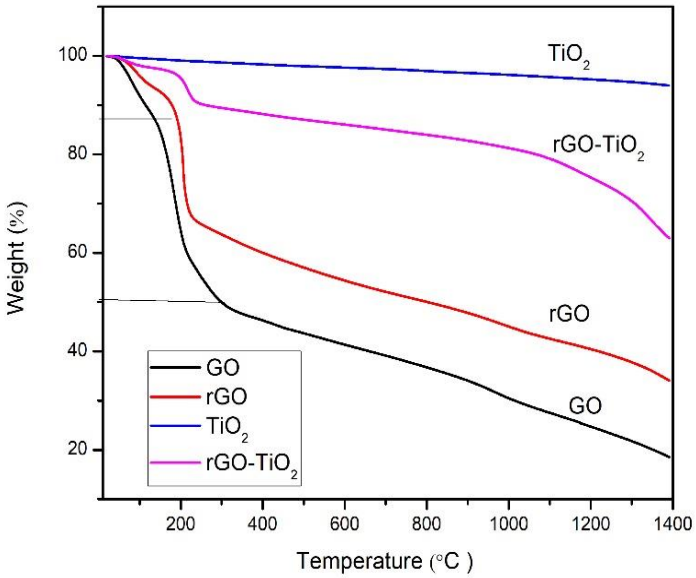

Figure 19: Thermogravimetric analysis of GO (black line), rGO (red line), rGO-TiO_2 (purple line) and TiO_2 (blue line).

It was shown from the Figure 19, that GO has a massive mass loss for heating at 1400°C. In the initial stage GO has gone through almost 50% of weight loss due to the evaporation of absorbed and bound water molecules before 100 °C [81] and pyrolysis of less stable (CO, CO_2, and H_2O) oxygenated functional groups above 100°C. The later mass loss (~32%) after 250°C can be attributed to the content of carbon and more stable oxygenated functional groups in GO carbon skeleton. The elimination of oxygen functional groups in GO, however, results in increased van der Waals forces between the layers of rGO, giving it better thermal stability than GO. Due to this rGO demonstrated a less total mass (~65%) loss compare to GO appeared in its TGA graphs because of partial reduction [91].

The TGA curve of TiO_2 show no noticeable weight loss up to 900 °C. In the 900 to 1400 °C range, small linear weight reductions were found. TiO_2 possess a high thermal stability as it has deconposed a very slight mass upon heating until 1400°C. When heated from room temperature to 1400°C, rGO-TiO_2 initial weight loss is due to the vaporization of water molecules that were absorbed. The last gradual mass loss at around 230°C is because of decomposition of carbon and residual oxygen functions Additionally, it shows that rGO-TiO_2 displayed superior thermal stability as a result of the strong interaction between TiO_2 and rGO sheets.

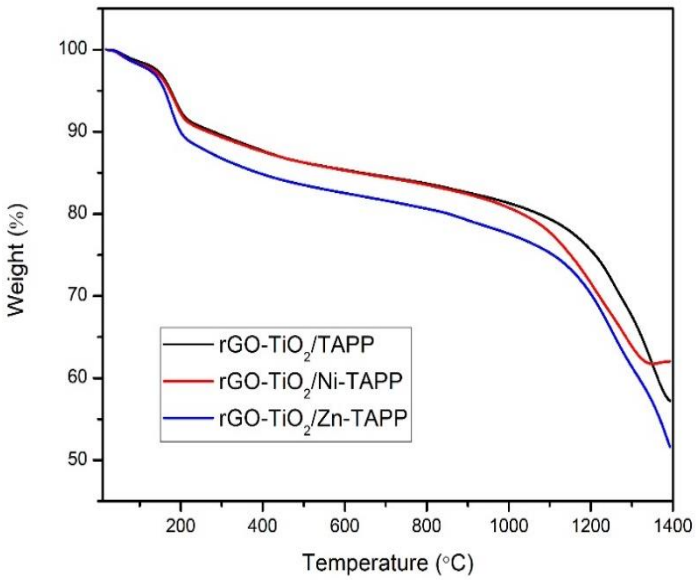

Figure 20: Thermogravimetric analysis of rGO-TiO_2/TAPP, rGO-TiO_2 /Ni-TAPP and rGO-TiO_2 /Zn-TAPP.

The TGA graph of the three hybrid nanocomposites (Figure 20) showed that the thermal stability of the three composite samples are almost similar. The 1st stage weight loss of the three samples around 100°C indicates water vaporization, whereas the 2nd step mass loss near 210°C could be attributed to the degradation of TAPP , Ni-TAPP and Zn-TAPP molecules covalently attached to the rGO-TiO_2 surface [81] .

3.6 UV-Visible Spectroscopy:

UV-Visible Spectroscopy were conducted to determine the optical properties and light absorption ability of the nanocomposite's samples. All the samples were diluted in DI water solution and DMF solution and tested with Agilent Cary 60 UV-Visible spectrophotometer. It should be noted that differences in concentration of the solution are to blame for the variations in the samples' overall absorption intensities.

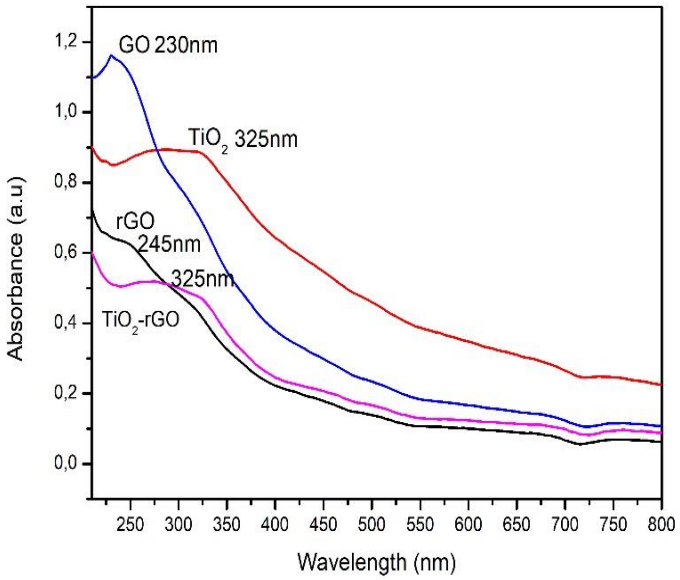

Figure 21:UV-vis spectra of GO,rGO,TiO_2 and rGO-TiO_2 in water solution.

In the UV-vis spectrum (Figure 21), a strong π– π * absorption band at 230 nm for GO is observed for C=C bond and a weak band at 300 nm attributed to n-π* absorption of C=O bond. This π– π * transition peak of GO red shifted to 245 nm for rGO, specifying the reduction of GO by removing of some groups on the GO surface. A 325 nm excitation absorption peak is visible in the UV-visible absorption peaks of TiO_2 and rGO-TiO_2 nanocomposites. From the UV-vis spectrum it can be stated that after the recombination of the π–π covalent bond of graphene sheets to TiO_2, rGO has improved the ability of TiO_2 to absorb visible light . Furthermore, rGO-TiO_2 has exhibited a broader red shifted absorbance peak compare to rGO [92] .

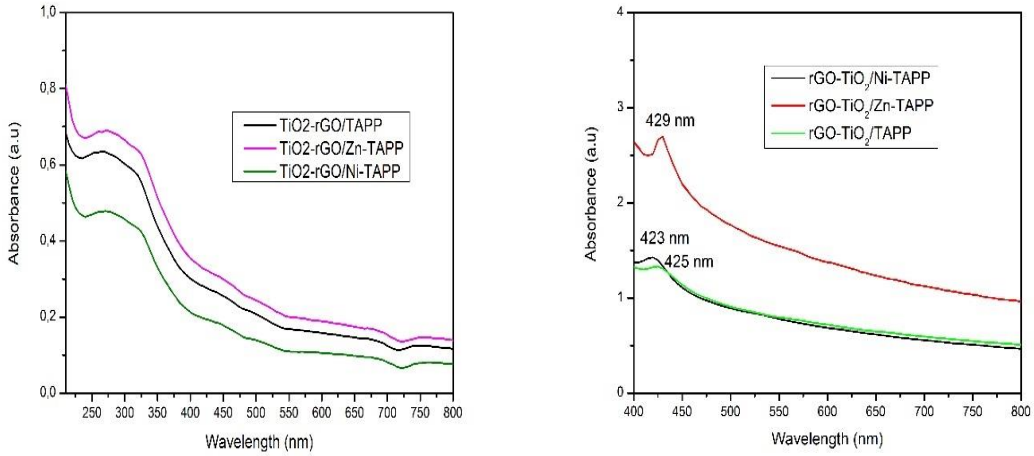

A) B)

Figure 22:UV-vis spectra of rGO-TiO_2 ,rGO-TiO_2/TAPP, rGO-TiO_2 /Ni-TAPP and rGO-TiO_2 /Zn-TAPP samples in A)water solution B) DMF solution

The low concentration of the samples rGO-TiO_2 ,rGO-TiO_2/TAPP, rGO-TiO_2 /Ni-TAPP and rGO-TiO_2 /Zn-TAPP were unable to provide strong, sharp and clearly detectable UV-vis absorbance band in water solution.

In case of organic solution DMF, the UV-vis spectra of the nanocomposites presented well defined absorption peaks in Figure 22. A strong absorbance were observed at 429 nm, 423 nm and 425 nm for the presence of Zn-TAPP , Ni-TAPP and TAPP metal porphyrin complexes respectively, that confirms the formation of rGO-TiO_2 /Zn-TAPP and rGO-TiO_2 /Ni-TAPP and rGO-TiO_2 /TAPP hybrid nanocomposites [93], [94].

4 Electrochemical Measurements for CO_2 reduction:

The electrochemical properties of all the synthesized nanocomposite materialsforCO_2 reduction were evaluated by using cyclic voltammetry (CV) technique. For conducting the electrochemical measurements, an one-compartment electrochemical cell setup with three electrodes was used (Figure 23).

The cell consists of a glassy carbon electrode as working electrode, Figure 23, Pt wire as a counter (auxiliary)electrode and a silver wire coated with AgCl used as a quasi-reference (QRE) electrode. The Ag/AgCl reference electrode was prepared by following a published procedure and externally calibrated by using ferrocenium/ferrocene redox couple (Fc^+/Fc) with a potential of 0.72 V against a normal hydrogen electrode as a reference value [95] .

The working electrode was polished after every CV with 6 μm,3 μm, 1 μm and ¼ μm diamond paste in ethanol and then rinsed, sonicated in ethanol to remove particulates, and rinsed with acetone before being dried under a nitrogen stream. The Pt wire was cleaned by burning and the reference electrode was rinsed and cleaned with DI water and ethanol before every measurement.

A potentiostat with Auto lab Nova 2.1.4 software was used for running all the cyclic voltammetry measurements.

The CVs measurements of all the composites were recorded in two different electrolyte solution to observe the electrochemical behavior of the synthesized catalysts in two different solvents. The solvent of one solution was dried acetonitrile which is an aprotic organic solvent with a dissolved 0.1 M tetrabutylammonium hexafluorophosphate ($TBAPF_6$) electrolyte. Another set of solution that was used for the CVs measurements of the prepared catalyst is potassium chloride (KCL) electrolyte dissolved in DI water.

The start and end potential were applied on the working electrode for all measurements were both -0.01 V while the upper vertex potential and lower vertex potential were 0.000 V and -2.5 V respectively, at as scan rate recorded at 100mV/sec. Current densities were measured using the working electrode's geometric area (3.0 mm^2).

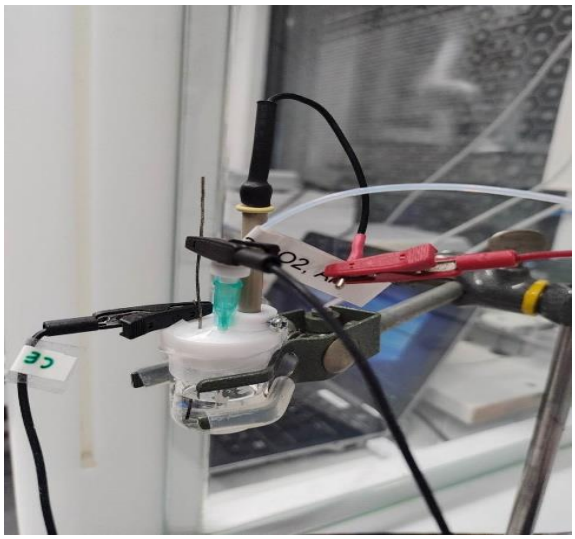

Figure 23: Three electrode cell containing electrochemical cell purging with gas.

Firstly, the prepared electrolyte solution was purged with N_2 gas for 10 minutes to remove all the dissolved gases. Then the electrochemical cell was filled up with 5 ml of the prepared electrolyte solution for each measurement. To make a comparison of N_2 atmosphere with CO_2, the solution was at first purged with N_2 gas for 30 minutes continuously at an ambient temperature and pressure (50 scc/m). After completing purging, current was measured against applied potential in N_2 saturated solution as the background. After that the electrolyte solution was purged with CO_2 gas for 30 minutes and the experiment was repeated with all the nanocomposites coated on GC electrode.

4.1 Cyclic Voltammetry measurements Of the Catalysts in Organic medium:

The CVs of TiO_2 in the Figure 24 demonstrated almost no current response under N_2 purged condition (black line) and zero catalytic activity for CO_2 reduction in CO_2 saturated state (red line). As mentioned previously, to improve the electro-conductivity of TiO_2 on CO_2 electro-reduction, rGO was combined to TiO_2. The CV of rGO-TiO_2 for N_2 purged (blue curve) solution has projected no catalytic activity. After purging the electrolytic solution of rGO-TiO_2 with CO_2 for 30 minutes, a high reduction current peak approximately -450 µA appeared at around -1.9V. The reduction started at a lower potential -1V which indicates the unique properties and large surface area of rGO has improved Titanium dioxide's electron conductivity

and the hybrid nanocomposite rGO-TiO_2 has a good positive electrocatalytic effect on CO_2 electro reduction.

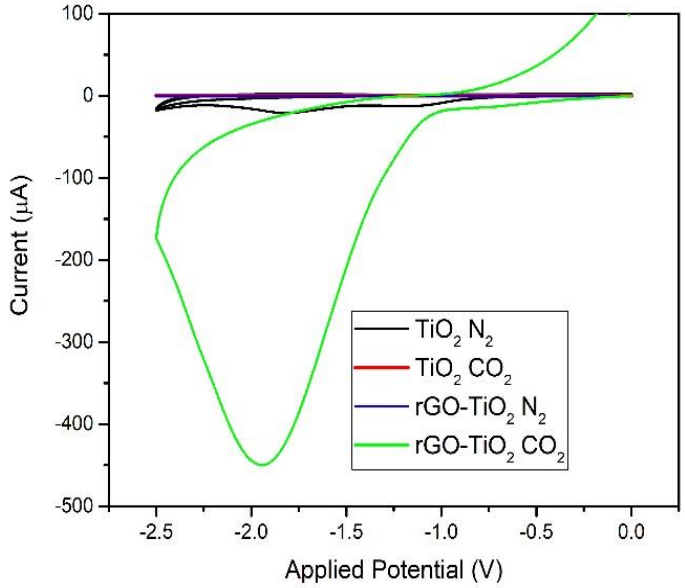

Figure 24: CV of TiO_2 (black and red curve) and rGO-TiO_2 coated electrode (blue and green curve) dipped into dried ACN containing 0.1M $TBAPF_6$ purging under N_2 and CO_2 saturated conditions, recorded at 100 mV/s scan rate from 0.00 to -2.5 V potential range.

In Figure 25, the cyclic voltammograms of the clean glassy carbon electrode, black curve (N_2 purged) and the red curve (CO_2 purged) showed no noticeable current response. In contrast, the CV (blue curve) of TiO_2-RGO/TAPP shows the current vs potential under N_2 saturated condition and it showed a lower current response (-118 μA) with a reduction peak at around -1.2 V. After purging CO_2 for 30 minutes into the electrolyte solution, a high cathodic current peak enhancement at around -1.8 V (green curve) was observed. The reduction started at a low reduction point at -1V .This reduction peak is indicating the successful electrochemical reduction of CO_2 on TiO_2 -RGO /TAPP hybrid nanocomposite coated GC working electrode through a noticeable current increment from -30 μA - 467 μA .

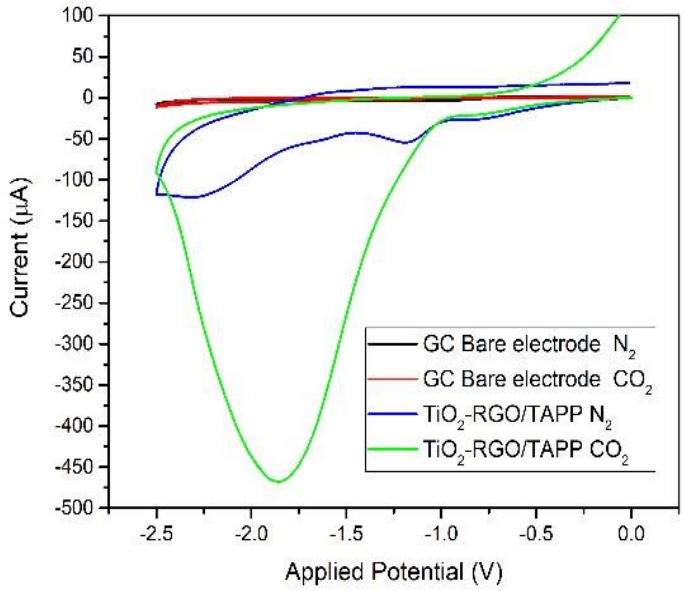

Figure 25: CVs of a clean GC electrode and a GC electrode coated with TiO_2- RGO/TAPP in the presence of 0.1M $TBAPF_6$ in dried ACN solution. Solution was purged 30 minutes before every measurement under N_2 (black and blue lines) and CO_2 saturated conditions (red and green lines) respectively at an ambient temperature and pressure (50 scc/m), recorded at 100 mV/s scan rate from 0.00 to -2.5 V..

In Figure 26 it seen that in comparison to the clean GC electrode, TiO_2-RG /Ni-TAPP coated working electrode in the presence of N_2 and CO_2 showed positive electrolytic activities. Whereas the bare GC electrode barely showed any current response in the same potential range in the presence of both N_2 and CO_2 atmosphere. The N_2 purged solution with TiO_2 -RGO /Ni-TAPP GC electrode showed reduction peaks with a lower current activities. However, a strong catalytic current enhancement approximately -343 μA of TiO_2 -RGO/Ni-TAPP at -1.8V was detected. In comparison to N_2 (blue curve) saturated condition the CO_2 reduction (green curve) has started at earlier potential point at around -0.99V which signifies, TiO_2 -RGO /Ni-TAPP hybrid catalyst has good catalytic effect for CO_2 electroreduction.

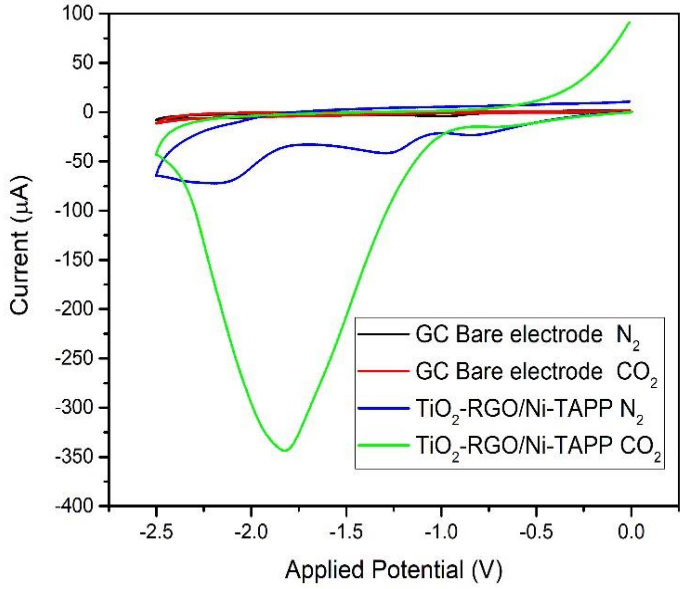

Figure 26: CVs of a clean GC working electrode (black and red lines) and a GC electrode coated with TiO_2-RGO/Ni-TAPP (blue and green curves) in 0.1M $TBAPF_6$ dried ACN solution at the presence N_2 and CO_2 gases for a 0.00 to -2.5 V potential range using a 100mV/s scan rate.

By comparing the CVs of a bare GC electrode with the TiO2-RGO/Zn-TAPP coated electrode shown in Figure 27 we can analyzed that the bare GC electrode has no current response but the presence of TiO_2-RGO/Zn-TAPP nanocomposite catalyst on the working electrode surface has clearly a better CO_2 electrocatalytic reduction performance. The current growth under N_2 saturated condition for TiO_2-RGO/Zn-TAPP catalyst (blue line) is much lower than CO_2 purged atmosphere. The CO_2 reduction has started at a lower applied potential (-0.92 V) with a high reduction current increment from -19 μA to -360 μA at -1.8V.

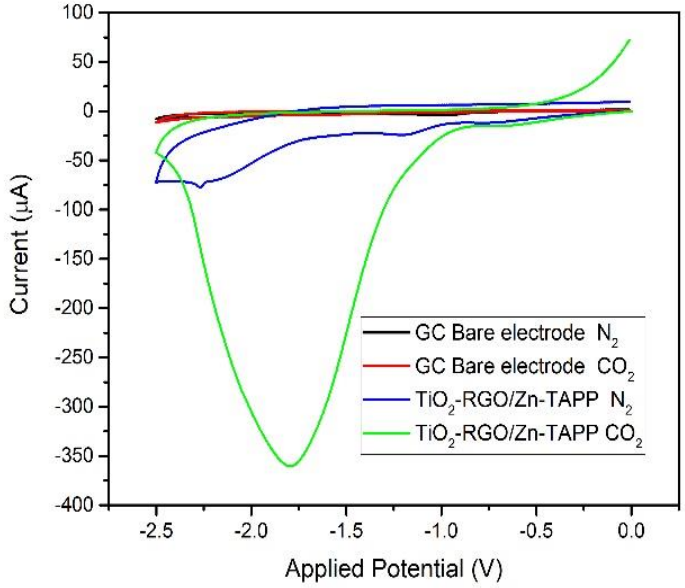

Figure 27: CVs of 0.1M $TBAPF_6$ solution in dried acetonitrile of a bare glassy carbon working electrode (black and red curves) and a GC electrode surface coated on TiO_2-RGO/Zn-TAPP (blue and green curves) nanocomposites for 0.00 to -2.5 V potential range at 100mV/s scan rate under N_2 and CO_2 purged conditions for 30 minutes before each electrolysis measurements at an ambient temperature and pressure (50 scc/m).

By comparing the CVs iigure 28, of the rGO-TiO_2 /TAPP nanocomposite with other two metalloporphyrin based catalysts, it can be concluded that rGO-TiO_2 /TAPP has better catalytic activity then the rGO-TiO_2 /Ni-TAPP and rGO-TiO_2 /Zn-TAPP composites. rGO-TiO_2 /TAPP coated catalyst starts reducing CO_2 at a less negativepotential at around -1 V whereas the other two composites starting point for CO_2 reduction was at -1.1V. rGO-TiO_2 /TAPP composite coated electrode gives a higher cathodic current signal compare to the other two hydro catalysts in the presence of CO_2, approximately (-468 μA) at a lower reduction potential which proves that rGO-TiO_2 /TAPP catalyst has enhanced the electrical conductivity for CO_2 electroreduction compare to other two metal based composites.

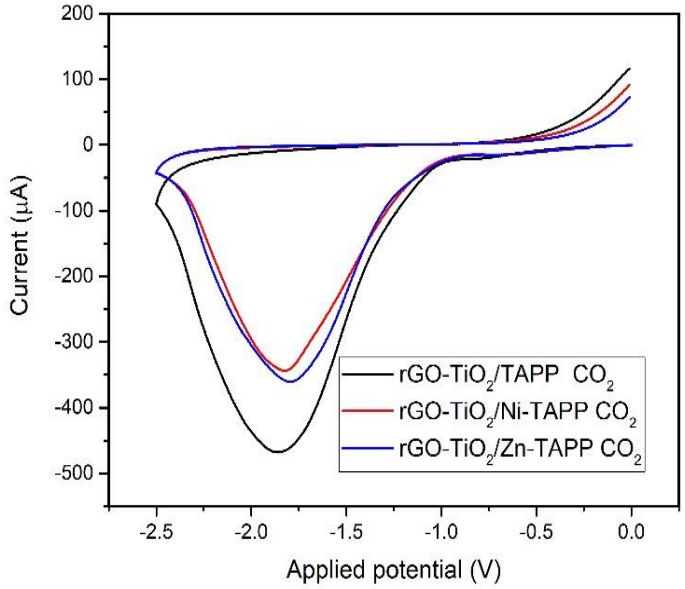

Figure 28: CVs of rGO-TiO_2 /TAPP (black curve), rGO-TiO_2 /Ni-TAPP (red curve) (rGO-TiO_2 /Zn-TAPP (blue curve) in a 0.1M $TBAPF_6$ organic solution containing dried ACN under the CO_2 saturated conditions (30 minutes purging) recorded at 100 mV/s scan rate with 0.00 to -2.5 V potential range at an ambient temperature and pressure (50 scc/m).

4.2 Cyclic Voltammetry measurements in aqueous medium:

In Figure 29, TiO_2 coated electrode shows undetermined oxidation activity in the potential range of -.2V to -1.6 V in N_2 (black curve) atmosphere and from 0 V to -1.2 V at CO_2 (red curve) in water solutions which could be attributed to the protonation process. A two-fold current decrease was observed under CO_2 saturated condition which suggests that compare to N_2 purged condition TiO_2 coated electrode display lower cathodic current activity for CO_2 electroreduction. To improve the catalytic activity for CO_2 reduction rGO was added with TiO_2. From the CVs of rGO-TiO_2 Figure 30 it was observed that under CO_2 purged condition rGO-TiO_2 coated electrode provided a better cathodic activity. The reduction started at a much less negative potential at around -.8V showing a high cathodic current response in compare to TiO_2 coated electrode at CO_2 ambience.We also observed that there was no obvious activity difference between blue (N_2) and green (CO_2) curve of rGO-TiO_2. So, it can be said that rGO-TiO_2 composite combination has improved theCO_2 electroreduction activity.

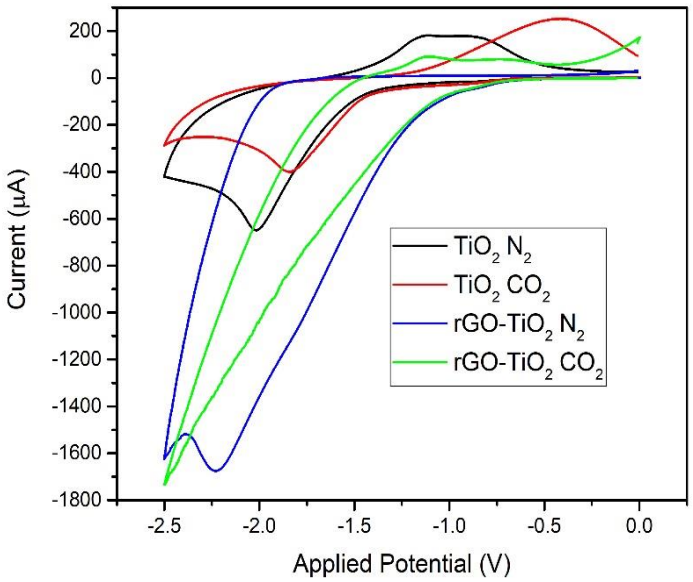

Figure 29: CVs of TiO_2 (black and red lines) and rGO-TiO_2 (blue and green curves) coated GC electrode in .01M H_2O (DI) solution containing KCL as at the presence N_2 and CO_2 gases for 0.00 to -2.5 V using a 100mV/s scan rate at ambient temperature and pressure (50scc/m).

In the Figure 30, it is clearly noticeable that the bare GC electrode in N_2 atmosphere (black curve) showed a low cathodic current signal (-388μA), whereas the red curve (CO_2 atmosphere) showed very low cathodic current response with an overpotential at around -1.9 V. There was no obvious activity difference noticed between blue (N_2 purged) and green curve (CO_2 purged) for rGO-TiO_2 /TAPP based composite material. But the reduction of CO_2 for rGO-TiO_2 /TAPP catalyst coated electrode has started at a much less negative potential at -1V with a big cathodic current enhancement from which we can stated that rGO-TiO_2 /TAPP catalyst has improved the catalytic activity for CO_2 electro reduction.

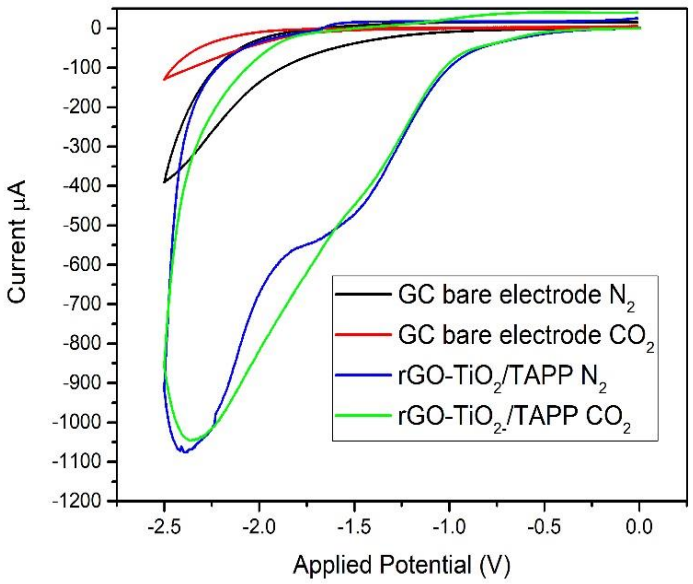

Figure 30: CVs of a bare GC electrode and a GC electrode coated with rGO-TiO_2 /TAPP in the presence of 0.01M H_2O (DI) solution containing KCL as electrolyte after 30 minutes purging before each measurement under N_2 (black and blue lines) and CO_2 saturated conditions (red and green lines), respectively at an ambient temperature and pressure (50 scc/m) , recorded at 100 mV/s scan rate within 0.00 to -2.5 V..

The TiO_2-RGO /Ni-TAPP catalyst coated electrode has presented Figure 31 an almost eight times bigger cathodic current response almost -1270µA in CO_2 purged condition (green curve) for CO_2 reduction which has started at a lower reduction point at around -0.81 V compare to the bare GC electrode at CO_2 atmosphere (red curve).This proves that TiO_2-RGO /Ni-TAPP hybrid catalyst has drastically improved the catalytic activity for electrochemical reduction of CO_2.

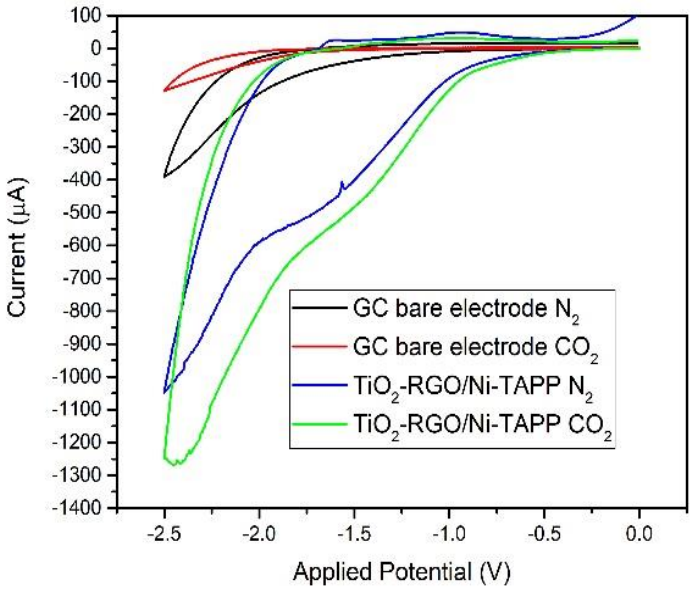

Figure 31: CVs of a clean GC working electrode (black and red lines) and a GC electrode coated with TiO_2-RGO/Ni-TAPP (blue and green curves) in 0.1 M aqueous KCL solution purged 30 minutes continuously with N_2 and CO_2 gases respectively at an ambient temperature and pressure (50 scc/m), for a 0.00 to -2.5 V Potential range using a 100mV/s scan rate.

The comparison of CO_2 electro-reduction performance between a bare GC electrode and rGO-TiO_2 /Zn-TAPP composite was witnessed clearly in Figure 32 under CO_2 saturated state GC electrode has a very low current response started at more negative reduction potentials at around -1.9V, although rGO-TiO_2 /Zn-TAPP coated electrode has demonstrated an increased cathodic current peak (CO_2 atmosphere) with a very less starting point at around -0.65V for CO_2 reduction. rGO-TiO_2 /Zn-TAPP composite has proved that it has a positive catalytic function for CO_2 electroreduction.

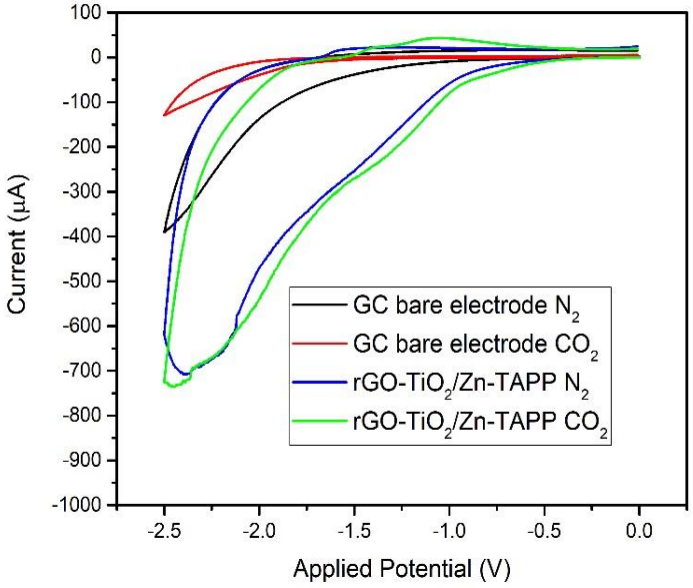

Figure 32: CVs of 0.1M KCL H_2O (DI) solution of a bare glassy carbon working electrode (black and red curves) and a GC electrode surface coated on rGO-TiO_2 /Zn-TAPP (blue and green curves) nanocomposites for 0.00 to -2.5V potential range at 100mV/s scan rate under N_2 and CO_2 purged conditions for 30 minutes before each electrolysis measurements at an ambient temperature and pressure(50 scc/m).

It can be seen from the CVs of the three hybrid catalysts that in comparison to rGO-TiO_2 /TAPP and rGO-TiO_2 /Zn-TAPP, rGO-TiO_2 /Ni-TAPP Figure 33 has better cathodic current response. Before running the CVs each electrolytic solution with the catalyst coated electrode was purged with CO_2 for 30 minutes. The reduction started at less negative reductionpotential in rGO-TiO_2 /Ni-TAPP at -0.82V with a higher current response approximately -1267 μA compare to the other two catalysts. We can conclude that in aqueous media rGO-TiO_2 /Ni-TAPP certainly has better performance for CO_2 electroreduction.

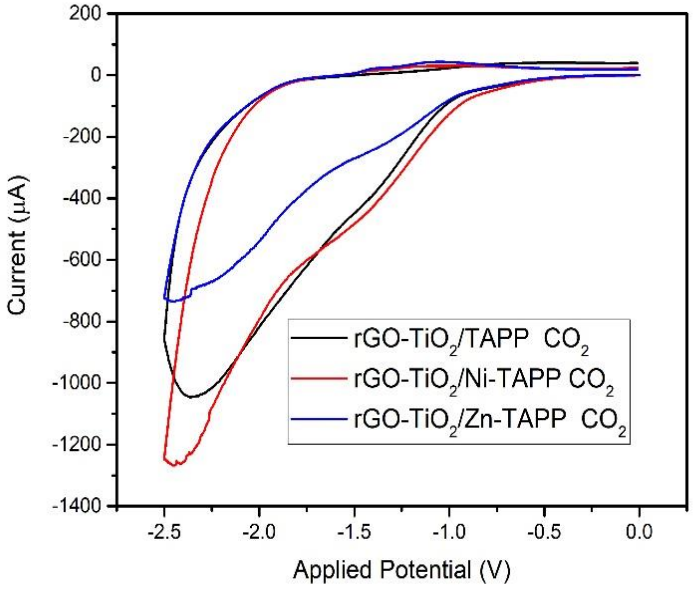

Figure 33 : CVs of rGO-TiO_2 /TAPP (black curve), rGO-TiO_2 /Ni-TAPP (red curve) and (rGO-TiO_2 /Zn-TAPP (blue curve) in a 0.1M KCL aqueous solution under the CO_2 saturated conditions (30 minutes purging) recorded at 100 mV/s scan rate with 0.00 to -2.5 V at an ambient temperature and pressure (50 scc/m).

5 CONCLUSION:

We successfully prepared three hybrid nanocomposites by combining rGO and TiO_2 with one porphyrin (TAPP) and two metalloporphyrin (Ni-TAPP & Zn-TAPP) complexes as catalysts for efficient CO_2 electroreduction along with a low CO_2 reduction potential and high current response which were main aim of this studies. All the samples were characterized by UV-visible, FTIR, Raman, XPS, TGA and XRD techniques to confirm the successful formation of the nanocomposites. The peaks of FTIR and XRD spectrum confirms the incorporation of the desired nanocomposite catalysts. In case of Raman spectra, the lower concentration of the porphyrin compounds loaded on rGO-TiO_2 couldn't provide noticeable Raman peak for detecting its presence and confirm aporphyrin complex formation. The thermal TGA studies showed good thermal stability of the synthesized catalysts. XPS analysis detected the existence of metals and other composite elements of the nanohybrid electrocatalysts confirming the successful synthesis of the composite materials. Generally,synergistic effect of rGO and metal porphyrins efficiently improve the electron conductivity by increase the electron hole pair separation and catalytic activity of catalyst. According to our CV results, we found that co sensitizing of rGO with TiO_2 and TAPP,ZnTAPP and Ni TAPP has greatly enhanced their CO_2 electroreduction activity in both water and organic medium compare to rGO-TiO_2 . Comparatively, high current response with low CO_2 reduction potential was observed in case of organic medium (Acetonitrile). rGO-TiO_2/Ni-TAPP drop-casted electrode showed a high cathodic current peak (-1300 μA) with a lower CO_2 reduction potential at around -.65 V in ACN solution. But in water solution rGO-TiO_2/Ni-TAPP CO_2 reduction applied potential was -0.92 V with a reduction current increased to -360 μA. This CO_2 reduction process were irreversible. On the basis of the CV results, it can be concluded that the synthesized hybrid nanocomposite have reduced the overpotential barrier needed for CO_2 reduction. In short, the produced nanocomposite catalysts have improved the CO_2 reduction performance as expected. Further study in this area could be an interesting topic to be researched.

References:

[1] R. Cassia, M. Nocioni, N. Correa-Aragunde, and L. Lamattina, "Climate change and the impact of greenhouse gasses: CO2 and NO, friends and foes of plant oxidative stress," *Frontiers in Plant Science*, vol. 9. Frontiers Media S.A., Mar. 01, 2018. doi: 10.3389/fpls.2018.00273.

[2] "Greenhouse gas emissions - Our World in Data." Accessed: Dec. 14, 2023. [Online]. Available: https://ourworldindata.org/greenhouse-gas-emissions

[3] D. Archer *et al.*, "Atmospheric lifetime of fossil fuel carbon dioxide," *Annual Review of Earth and Planetary Sciences*, vol. 37. pp. 117–134, May 2009. doi: 10.1146/annurev.earth.031208.100206.

[4] S. J. Davis, K. Caldeira, and H. D. Matthews, "Future CO2 emissions and climate change from existing energy infrastructure," *Science*, vol. 329, no. 5997, pp. 1330–1333, Sep. 2010, doi: 10.1126/SCIENCE.1188566.

[5] "Global CO2 emissions from fossil fuels at new record in 2022 | World Economic Forum." Accessed: Dec. 21, 2023. [Online]. Available: https://www.weforum.org/agenda/2022/11/global-co2-emissions-fossil-fuels-hit-record-2022/

[6] "CO2 Emissions in 2022 – Analysis - IEA." Accessed: Dec. 21, 2023. [Online]. Available: https://www.iea.org/articles/co2-emissions-in-2022

[7] T. Ahmad and D. Zhang, "A critical review of comparative global historical energy consumption and future demand: The story told so far," *Energy Reports*, vol. 6. Elsevier Ltd, pp. 1973–1991, Nov. 01, 2020. doi: 10.1016/j.egyr.2020.07.020.

[8] D. Gao, W. Li, H. Wang, G. Wang, and R. Cai, "Heterogeneous Catalysis for CO2 Conversion into Chemicals and Fuels," *Transactions of Tianjin University*, vol. 28, no. 4. Tianjin University, pp. 245–264, Aug. 01, 2022. doi: 10.1007/s12209-022-00326-x.

[9] S. Roy, A. Cherevotan, and S. C. Peter, "Thermochemical CO2 Hydrogenation to Single Carbon Products: Scientific and Technological Challenges," *ACS Energy Lett*, vol. 3, no. 8, pp. 1938–1966, Aug. 2018, doi: 10.1021/acsenergylett.8b00740.

[10] J. Shi *et al.*, "Enzymatic conversion of carbon dioxide †," *Chem. Soc. Rev*, vol. 44, p. 5981, 2015, doi: 10.1039/c5cs00182j.

[11] J. Grodkowski and P. Neta, "Copper-Catalyzed Radiolytic Reduction of CO 2 to CO in Aqueous Solutions," 2001, doi: 10.1021/jp004567d.

[12] B. Kumar, M. Llorente, J. Froehlich, T. Dang, A. Sathrum, and C. P. Kubiak, "Photochemical and photoelectrochemical reduction of CO2," *Annual Review of Physical Chemistry*, vol. 63. Annual Reviews Inc., pp. 541–569, 2012. doi: 10.1146/annurev-physchem-032511-143759.

[13] N. Han, P. Ding, L. He, Y. Li, and Y. Li, "Promises of Main Group Metal–Based Nanostructured Materials for Electrochemical CO2 Reduction to Formate," *Adv Energy Mater*, vol. 10, no. 11, Mar. 2020, doi: 10.1002/AENM.201902338.

[14] Z. Sun, T. Ma, H. Tao, Q. Fan, and B. Han, “Fundamentals and Challenges of Electrochemical CO2 Reduction Using Two-Dimensional Materials,” *Chem*, vol. 3, no. 4. Elsevier Inc, pp. 560–587, Oct. 12, 2017. doi: 10.1016/j.chempr.2017.09.009.

[15] W. Zhang *et al.*, “Progress and Perspective of Electrocatalytic CO2 Reduction for Renewable Carbonaceous Fuels and Chemicals,” *Advanced Science*, vol. 5, no. 1. Wiley-VCH Verlag, Jan. 01, 2018. doi: 10.1002/advs.201700275.

[16] A. Call, M. Cibian, K. Yamamoto, T. Nakazono, K. Yamauchi, and K. Sakai, “Highly Efficient and Selective Photocatalytic CO 2 Reduction to CO in Water by a Cobalt Porphyrin Molecular Catalyst,” 2019, doi: 10.1021/acscatal.8b04975.

[17] Y. Wu, Y. Liang, and H. Wang, “Heterogeneous Molecular Catalysts of Metal Phthalocyanines for Electrochemical CO2Reduction Reactions,” *Acc Chem Res*, vol. 54, no. 16, pp. 3149–3159, Aug. 2021, doi: 10.1021/ACS.ACCOUNTS.1C00200.

[18] J. D. Froehlich and C. P. Kubiak, “The Homogeneous Reduction of CO2 by [Ni(cyclam)]+: Increased Catalytic Rates with the Addition of a CO Scavenger,” *J Am Chem Soc*, vol. 137, no. 10, pp. 3565–3573, Mar. 2015, doi: 10.1021/JA512575V.

[19] N. Mie Elgrishi, M. B. Chambers, X. Wang, and M. Fontecave, “Molecular polypyridine-based metal complexes as catalysts for the reduction of CO 2,” *Chem. Soc. Rev*, vol. 46, p. 761, 2017, doi: 10.1039/c5cs00391a.

[20] H. Takeda, C. Cometto, O. Ishitani, and M. Robert, “Electrons, Photons, Protons and Earth-Abundant Metal Complexes for Molecular Catalysis of CO2 Reduction,” *ACS Catal*, vol. 7, no. 1, pp. 70–88, Jan. 2017, doi: 10.1021/ACSCATAL.6B02181.

[21] L. H. Vieira *et al.*, “Noble Metals in Recent Developments of Heterogeneous Catalysts for CO2 Conversion Processes,” *ChemCatChem*, vol. 15, no. 14, Jul. 2023, doi: 10.1002/CCTC.202300493.

[22] H. M. Castro-Cruz and N. A. Macías-Ruvalcaba, “Porphyrin-catalyzed electrochemical hydrogen evolution reaction. Metal-centered and ligand-centered mechanisms,” *Coord Chem Rev*, vol. 458, May 2022, doi: 10.1016/j.ccr.2022.214430.

[23] A. Li, S. Chen, F. Yang, H. Gao, C. Dong, and G. Wang, “Metalloporphyrin-Decorated Titanium Dioxide Nanosheets for Efficient Photocatalytic Carbon Dioxide Reduction,” vol. 22, p. 1, 2023, doi: 10.1021/acs.inorgchem.1c02957.

[24] S. Hiroto, Y. Miyake, and H. Shinokubo, “Synthesis and Functionalization of Porphyrins through Organometallic Methodologies,” *Chemical Reviews*, vol. 117, no. 4. American Chemical Society, pp. 2910–3043, Feb. 22, 2017. doi: 10.1021/acs.chemrev.6b00427.

[25] Y. Y. Birdja, J. Shen, and M. T. M. Koper, “Influence of the metal center of metalloprotoporphyrins on the electrocatalytic CO2 reduction to formic acid,” *Catal Today*, vol. 288, pp. 37–47, 2017, doi: 10.1016/j.cattod.2017.02.046.

[26] L. Cook, G. Brewer, and W. Wong-Ng, “Structural aspects of porphyrins for functional materials applications,” *Crystals*, vol. 7, no. 7. MDPI AG, Jul. 15, 2017. doi: 10.3390/cryst7070223.

[27] M. Imran, M. Ramzan, A. K. Qureshi, M. Azhar Khan, and M. Tariq, “Emerging applications of porphyrins and metalloporphyrins in biomedicine and diagnostic magnetic resonance imaging,” *Biosensors*, vol. 8, no. 4. MDPI, Oct. 19, 2018. doi: 10.3390/bios8040095.

[28] J. M. Gonçalves, T. A. Matias, L. Angnes, P. R. Martins, and K. Araki, “Review—Tetraruthenated Porphyrins and Composites as Catalysts and Sensor Materials: A Short Review,” *ECS Journal of Solid State Science and Technology*, vol. 9, no. 6, p. 061011, Jan. 2020, doi: 10.1149/2162-8777/ABA4F5.

[29] M. S. Sudi *et al.*, “Efficient photoelectrochemical water splitting of metal-porphyrin decorated on BiVO4 photoanode,” *Appl Surf Sci*, vol. 606, Dec. 2022, doi: 10.1016/J.APSUSC.2022.154753.

[30] Z. Liang *et al.*, “Metal–Organic-Framework-Supported Molecular Electrocatalysis for the Oxygen Reduction Reaction,” *Angewandte Chemie - International Edition*, vol. 60, no. 15, pp. 8472–8476, Apr. 2021, doi: 10.1002/ANIE.202016024.

[31] J. R. Stroka, B. Kandemir, E. M. Matson, and K. L. Bren, “Electrocatalytic Multielectron Nitrite Reduction in Water by an Iron Complex,” *ACS Catal*, vol. 10, no. 23, pp. 13968–13972, Dec. 2020, doi: 10.1021/ACSCATAL.0C03600/SUPPL_FILE/CS0C03600_SI_001.PDF.

[32] R. Chen *et al.*, “Rational design of isostructural 2D porphyrin-based covalent organic frameworks for tunable photocatalytic hydrogen evolution,” *Nature Communications 2021 12:1*, vol. 12, no. 1, pp. 1–9, Mar. 2021, doi: 10.1038/s41467-021-21527-3.

[33] J. Dong, X. Han, Y. Liu, H. Li, and Y. Cui, “Metal–Covalent Organic Frameworks (MCOFs): A Bridge Between Metal–Organic Frameworks and Covalent Organic Frameworks,” *Angewandte Chemie - International Edition*, vol. 59, no. 33, pp. 13722–13733, Aug. 2020, doi: 10.1002/ANIE.202004796.

[34] I. Bhugun, D. Lexa, and J. M. Savéant, “Ultraefficient Selective Homogeneous Catalysis of the Electrochemical Reduction of Carbon Dioxide by an Iron(0) Porphyrin Associated with a Weak Brönsted Acid Cocatalyst,” *J Am Chem Soc*, vol. 116, no. 11, pp. 5015–5016, Jun. 1994, doi: 10.1021/JA00090A068.

[35] I. Bhugun, D. Lexa, and J. M. Savéant, “Catalysis of the electrochemical reduction of carbon dioxide by iron(0) porphyrins: Synergystic effect of weak Brönsted acids,” *J Am Chem Soc*, vol. 118, no. 7, pp. 1769–1776, Feb. 1996, doi: 10.1021/JA9534462/ASSET/IMAGES/MEDIUM/JA9534462H00003.GIF.

[36] C. Costentin, M. Robert, and J. M. Savéant, “Current Issues in Molecular Catalysis Illustrated by Iron Porphyrins as Catalysts of the CO2-to-CO Electrochemical Conversion,” *Acc Chem Res*, vol. 48, no. 12, pp. 2996–3006, Nov. 2015, doi: 10.1021/ACS.ACCOUNTS.5B00262.

[37] I. Hod, M. D. Sampson, P. Deria, C. P. Kubiak, O. K. Farha, and J. T. Hupp, “Fe-Porphyrin-Based Metal-Organic Framework Films as High-Surface Concentration, Heterogeneous Catalysts for Electrochemical Reduction of CO2,” *ACS Catal*, vol. 5, no. 11, pp. 6302–6309, Nov. 2015, doi: 10.1021/acscatal.5b01767.

[38] X. Hu, M. H. Rønne, S. U. Pedersen, T. Skrydstrup, and K. Daasbjerg, “ Enhanced Catalytic Activity of Cobalt Porphyrin in CO 2 Electroreduction upon Immobilization on Carbon Materials ,” *Angewandte Chemie*, vol. 129, no. 23, pp. 6568–6572, Jun. 2017, doi: 10.1002/ANGE.201701104.

[39] S. Lin *et al.*, “Covalent organic frameworks comprising cobalt porphyrins for catalytic CO2 reduction in water,” *Science (1979)*, vol. 349, no. 6253, pp. 1208–1213, Sep. 2015, doi: 10.1126/SCIENCE.AAC8343/SUPPL_FILE/LIN.SM.PDF.

[40] A. Fujishima and K. Honda, “Electrochemical Photolysis of Water at a Semiconductor Electrode,” *Nature 1972 238:5358*, vol. 238, no. 5358, pp. 37–38, 1972, doi: 10.1038/238037a0.

[41] X. Chen and S. S. Mao, “Titanium dioxide nanomaterials: Synthesis, properties, modifications and applications,” *Chem Rev*, vol. 107, no. 7, pp. 2891–2959, Jul. 2007, doi: 10.1021/CR0500535.

[42] I. Ali, M. Suhail, Z. A. Alothman, and A. Alwarthan, “Recent advances in syntheses, properties and applications of TiO2 nanostructures,” *RSC Advances*, vol. 8, no. 53. Royal Society of Chemistry, pp. 30125–30147, 2018. doi: 10.1039/c8ra06517a.

[43] A. Weir, P. Westerhoff, L. Fabricius, K. Hristovski, and N. Von Goetz, “Titanium dioxide nanoparticles in food and personal care products,” *Environ Sci Technol*, vol. 46, no. 4, pp. 2242–2250, Feb. 2012, doi: 10.1021/ES204168D.

[44] N. T. Padmanabhan and H. John, “Titanium dioxide based self-cleaning smart surfaces: A short review,” *J Environ Chem Eng*, vol. 8, no. 5, Oct. 2020, doi: 10.1016/j.jece.2020.104211.

[45] D. Ziental *et al.*, “Titanium dioxide nanoparticles: Prospects and applications in medicine,” *Nanomaterials*, vol. 10, no. 2. MDPI AG, Feb. 01, 2020. doi: 10.3390/nano10020387.

[46] G. L. Chiarello, M. V. Dozzi, and E. Selli, “TiO2-based materials for photocatalytic hydrogen production,” *Journal of Energy Chemistry*, vol. 26, no. 2. Elsevier B.V., pp. 250–258, Mar. 01, 2017. doi: 10.1016/j.jechem.2017.02.005.

[47] M. Ge *et al.*, “A review of one-dimensional TiO2 nanostructured materials for environmental and energy applications,” *J Mater Chem A Mater*, vol. 4, no. 18, pp. 6772–6801, May 2016, doi: 10.1039/C5TA09323F.

[48] S. Paul, M. A. Rahman, S. Bin Sharif, J. H. Kim, S. E. T. Siddiqui, and M. A. M. Hossain, “TiO2 as an Anode of High-Performance Lithium-Ion Batteries: A Comprehensive Review towards Practical Application,” *Nanomaterials*, vol. 12, no. 12. MDPI, Jun. 01, 2022. doi: 10.3390/nano12122034.

[49] M. Mhadhbi, H. Abderazzak, and B. Avar, “Synthesis and Properties of Titanium Dioxide Nanoparticles,” *Updates on Titanium Dioxide*, Aug. 2023, doi: 10.5772/INTECHOPEN.111577.

[50] T. Luttrell, S. Halpegamage, J. Tao, A. Kramer, E. Sutter, and M. Batzill, “Why is anatase a better photocatalyst than rutile? - Model studies on epitaxial TiO2 films,” *Sci Rep*, vol. 4, Apr. 2015, doi: 10.1038/srep04043.

[51] J. Jia, L. Mu, Y. Lin, and X. Zhou, “Rutile versus anatase for quantum dot sensitized solar cell,” *Electrochim Acta*, vol. 266, pp. 103–109, Mar. 2018, doi: 10.1016/j.electacta.2018.01.186.

[52] J. Jia, H. Yamamoto, T. Okajima, and Y. Shigesato, “On the Crystal Structural Control of Sputtered TiO 2 Thin Films,” 2016, doi: 10.1186/s11671-016-1531-5.

[53] S. Bagheri, N. Muhd Julkapli, and S. Bee Abd Hamid, “Titanium dioxide as a catalyst support in heterogeneous catalysis,” *Scientific World Journal*, vol. 2014, 2014, doi: 10.1155/2014/727496.

[54] J. Moma, J. Baloyi, J. Moma, and J. Baloyi, “Modified Titanium Dioxide for Photocatalytic Applications,” *Photocatalysts - Applications and Attributes*, Nov. 2018, doi: 10.5772/INTECHOPEN.79374.

[55] Z. Luo *et al.*, “Crystalline mixed phase (anatase/rutile) mesoporous titanium dioxides for visible light photocatalytic activity,” *Chemistry of Materials*, vol. 27, no. 1, pp. 6–17, Jan. 2015, doi: 10.1021/CM5035112/ASSET/IMAGES/LARGE/CM-2014-035112_0008.JPEG.

[56] J. Yuan, M. P. Yang, Q. L. Hu, S. M. Li, H. Wang, and J. X. Lu, “Cu/TiO2 nanoparticles modified nitrogen-doped graphene as a highly efficient catalyst for the selective electroreduction of CO2 to different alcohols,” *Journal of CO2 Utilization*, vol. 24, pp. 334–340, Mar. 2018, doi: 10.1016/J.JCOU.2018.01.021.

[57] Y. Chen, C. W. Li, and M. W. Kanan, “Aqueous CO2 reduction at very low overpotential on oxide-derived au nanoparticles,” *J Am Chem Soc*, vol. 134, no. 49, pp. 19969–19972, Dec. 2012, doi: 10.1021/JA309317U/ASSET/IMAGES/LARGE/JA-2012-09317U_0002.JPEG.

[58] M. N. Hossain, R. M. Choueiri, S. Abner, L. D. Chen, and A. Chen, “Electrochemical Reduction of Carbon Dioxide at TiO2/Au Nanocomposites,” *ACS Appl Mater Interfaces*, vol. 14, no. 46, pp. 51889–51899, Nov. 2022, doi: 10.1021/acsami.2c14368.

[59] F. Farjadian *et al.*, “Recent Developments in Graphene and Graphene Oxide: Properties, Synthesis, and Modifications: A Review,” *ChemistrySelect*, vol. 5, no. 33. Wiley-Blackwell, pp. 10200–10219, Sep. 07, 2020. doi: 10.1002/slct.202002501.

[60] D. G. Papageorgiou, I. A. Kinloch, and R. J. Young, “Mechanical properties of graphene and graphene-based nanocomposites,” *Progress in Materials Science*, vol. 90. Elsevier Ltd, pp. 75–127, Oct. 01, 2017. doi: 10.1016/j.pmatsci.2017.07.004.

[61] A. R. Monteiro, M. G. P. M. S. Neves, and T. Trindade, “Functionalization of Graphene Oxide with Porphyrins: Synthetic Routes and Biological Applications,” *ChemPlusChem*, vol. 85, no. 8. Wiley-VCH Verlag, pp. 1857–1880, Aug. 01, 2020. doi: 10.1002/cplu.202000455.

[62] S. J. Lee, S. J. Yoon, and I. Y. Jeon, “Graphene/Polymer Nanocomposites: Preparation, Mechanical Properties, and Application,” *Polymers (Basel)*, vol. 14, no. 21, Nov. 2022, doi: 10.3390/POLYM14214733.

[63] S. Choi, C. Kim, J. M. Suh, and H. W. Jang, “Reduced graphene oxide-based materials for electrochemical energy conversion reactions,” *Carbon Energy*, vol. 1, no. 1. Blackwell Publishing Inc., pp. 85–108, Sep. 01, 2019. doi: 10.1002/cey2.13.

[64] A. T. Smith, A. M. LaChance, S. Zeng, B. Liu, and L. Sun, “Synthesis, properties, and applications of graphene oxide/reduced graphene oxide and their nanocomposites,” *Nano Materials Science*, vol. 1, no. 1, pp. 31–47, Mar. 2019, doi: 10.1016/j.nanoms.2019.02.004.

[65] R. Tarcan, O. Todor-Boer, I. Petrovai, C. Leordean, S. Astilean, and I. Botiz, “Reduced graphene oxide today,” *J Mater Chem C Mater*, vol. 8, no. 4, pp. 1198–1224, Jan. 2020, doi: 10.1039/C9TC04916A.

[66] T. Tsujiguchi *et al.*, “Acceleration of electrochemical CO2 reduction to formate at the Sn/ reduced graphene oxide interface,” *ACS Catal*, vol. 11, no. 6, pp. 3310–3318, Mar. 2021, doi: 10.1021/ACSCATAL.0C04887/ASSET/IMAGES/ACSCATAL.0C04887.SOCIAL.JPEG_V03 .

[67] H. Y. Jeong *et al.*, “Tris(2-benzimidazolylmethyl)amine-Directed Synthesis of Single-Atom Nickel Catalysts for Electrochemical CO Production from CO2,” *Chemistry - A European Journal*, vol. 24, no. 69, pp. 18444–18454, Dec. 2018, doi: 10.1002/chem.201803615.

[68] S. Jin, Z. Hao, K. Zhang, Z. Yan, and J. Chen, “Advances and Challenges for the Electrochemical Reduction of CO2 to CO: From Fundamentals to Industrialization,” *Angewandte Chemie - International Edition*, vol. 60, no. 38, pp. 20627–20648, Sep. 2021, doi: 10.1002/ANIE.202101818.

[69] C. A. R. Pappijn, M. Ruitenbeek, M. F. Reyniers, and K. M. Van Geem, “Challenges and Opportunities of Carbon Capture and Utilization: Electrochemical Conversion of CO2 to Ethylene,” *Front Earth Sci (Lausanne)*, vol. 8, Sep. 2020, doi: 10.3389/fenrg.2020.557466.

[70] S. Overa, B. H. Ko, Y. Zhao, and F. Jiao, “Electrochemical Approaches for CO2 Conversion to Chemicals: A Journey toward Practical Applications,” *Acc Chem Res*, vol. 55, no. 5, pp. 638–648, Mar. 2022, doi: 10.1021/ACS.ACCOUNTS.1C00674/ASSET/IMAGES/ACS.ACCOUNTS.1C00674.SOCIAL .JPEG_V03.

[71] X. M. Hu, S. U. Pedersen, and K. Daasbjerg, “Supported molecular catalysts for the heterogeneous CO2 electroreduction,” *Current Opinion in Electrochemistry*, vol. 15. Elsevier B.V., pp. 148–154, Jun. 01, 2019. doi: 10.1016/j.coelec.2019.05.006.

[72] O. S. Bushuyev *et al.*, “What Should We Make with CO2 and How Can We Make It?,” *Joule*, vol. 2, no. 5. Cell Press, pp. 825–832, May 16, 2018. doi: 10.1016/j.joule.2017.09.003.

[73] F. Yu, K. Deng, M. Du, W. Wang, F. Liu, and D. Liang, “Electrochemical CO2 reduction: From catalysts to reactive thermodynamics and kinetics,” *Carbon Capture Science and Technology*, vol. 6. Elsevier Ltd, Mar. 01, 2023. doi: 10.1016/j.ccst.2022.100081.

[74] Q. Lu and F. Jiao, “Electrochemical CO 2 reduction: electrocatalyst, reaction mechanism, and process engineering,” 2016.

[75] J. Rosen *et al.*, “Mechanistic Insights into the Electrochemical Reduction of CO2 to CO on Nanostructured Ag Surfaces,” *ACS Catal*, vol. 5, no. 7, pp. 4293–4299, Jun. 2015, doi: 10.1021/ACSCATAL.5B00840.

[76] M. Wang *et al.*, “CO 2 electrochemical catalytic reduction with a highly active cobalt phthalocyanine”, doi: 10.1038/s41467-019-11542-w.

[77] A. Klinkova *et al.*, “Rational Design of Efficient Palladium Catalysts for Electroreduction of Carbon Dioxide to Formate,” *ACS Catal*, vol. 6, no. 12, pp. 8115–8120, Dec. 2016, doi: 10.1021/ACSCATAL.6B01719/ASSET/IMAGES/ACSCATAL.6B01719.SOCIAL.JPEG_V03 .

[78] S. Sarfraz, A. T. Garcia-Esparza, A. Jedidi, L. Cavallo, and K. Takanabe, “Cu-Sn Bimetallic Catalyst for Selective Aqueous Electroreduction of CO2 to CO,” *ACS Catal*, vol. 6, no. 5, pp. 2842–2851, May 2016, doi: 10.1021/acscatal.6b00269.

[79] N. Kornienko *et al.*, “Metal-organic frameworks for electrocatalytic reduction of carbon dioxide,” *J Am Chem Soc*, vol. 137, no. 44, pp. 14129–14135, Nov. 2015, doi: 10.1021/JACS.5B08212.

[80] M. Hirata, T. Gotou, S. Horiuchi, M. Fujiwara, and M. Ohba, “Thin-film particles of graphite oxide 1: High-yield synthesis and flexibility of the particles,” *Carbon N Y*, vol. 42, no. 14, pp. 2929–2937, 2004, doi: 10.1016/j.carbon.2004.07.003.

[81] S. Kumar, R. K. Yadav, K. Ram, A. Aguiar, J. Koh, and A. J. F. N. Sobral, “Graphene oxide modified cobalt metallated porphyrin photocatalyst for conversion of formic acid from carbon dioxide,” *Journal of CO2 Utilization*, vol. 27, pp. 107–114, Oct. 2018, doi: 10.1016/j.jcou.2018.07.008.

[82] M. Wei, J. Wan, Z. Hu, Z. Peng, and B. Wang, “Enhanced photocatalytic degradation activity over TiO 2 nanotubes co-sensitized by reduced graphene oxide and copper(II) meso-tetra(4-carboxyphenyl)porphyrin,” *Appl Surf Sci*, vol. 377, pp. 149–158, Jul. 2016, doi: 10.1016/j.apsusc.2016.03.120.

[83] M. Bera, Chandravati, P. Gupta, and P. K. Maji, “Facile One-Pot Synthesis of Graphene Oxide by Sonication Assisted Mechanochemical Approach and Its Surface Chemistry,” *J Nanosci Nanotechnol*, vol. 18, no. 2, pp. 902–912, Sep. 2017, doi: 10.1166/JNN.2018.14306.

[84] M. Al-Amin, S. Chandra Dey, T. U. Rashid, M. Ashaduzzaman, and S. M. Shamsuddin, "Solar Assisted Photocatalytic Degradation of Reactive Azo Dyes in Presence of Anatase Titanium Dioxide," *International Journal of Latest Research in Engineering and Technology (IJLRET*, vol. 2, pp. 14–21, 2016, [Online]. Available: www.ijlret.com‖www.ijlret.com

[85] L. Wang *et al.*, "Anchored Cu(II) tetra(4-carboxylphenyl)porphyrin to P25 (TiO2) for efficient photocatalytic ability in CO2 reduction," *Appl Catal B*, vol. 239, pp. 599–608, Dec. 2018, doi: 10.1016/j.apcatb.2018.08.007.

[86] R. Muzyka, S. Drewniak, T. Pustelny, M. Chrubasik, and G. Gryglewicz, "Characterization of Graphite Oxide and Reduced Graphene Oxide Obtained from Different Graphite Precursors and Oxidized by Different Methods Using Raman Spectroscopy," *Materials 2018, Vol. 11, Page 1050*, vol. 11, no. 7, p. 1050, Jun. 2018, doi: 10.3390/MA11071050.

[87] J. L. Xochihua Juan *et al.*, "TiO2 doped with europium (Eu): Synthesis, characterization and catalytic performance on pesticide degradation under solar irradiation," *Catal Today*, vol. 394–396, pp. 304–313, Jul. 2022, doi: 10.1016/j.cattod.2021.08.024.

[88] H. Gao *et al.*, "Construction of TiO2 nanosheets/tetra (4-carboxyphenyl) porphyrin hybrids for efficient visible-light photoreduction of CO2," *Chemical Engineering Journal*, vol. 374, pp. 684–693, Oct. 2019, doi: 10.1016/j.cej.2019.06.002.

[89] M. Tayebi, M. Kolaei, A. Tayyebi, Z. Masoumi, Z. Belbasi, and B. K. Lee, "Reduced graphene oxide (RGO) on TiO2 for an improved photoelectrochemical (PEC) and photocatalytic activity," *Solar Energy*, vol. 190, pp. 185–194, Sep. 2019, doi: 10.1016/j.solener.2019.08.020.

[90] S. Kochrekar *et al.*, "Copolymers of bipyridinium and metal (Zn & Ni) porphyrin derivatives; theoretical insights and electrochemical activity towards CO 2 †," 2021, doi: 10.1039/d1ra01945g.

[91] T. Tene *et al.*, "Toward large-scale production of oxidized graphene," *Nanomaterials*, vol. 10, no. 2, Feb. 2020, doi: 10.3390/nano10020279.

[92] X. Qi, S. Zhang, T. Wang, S. Guo, and R. Ren, "Effect of high-dispersible graphene on the strength and durability of cement mortars," *Materials*, vol. 14, no. 4, pp. 1–17, Feb. 2021, doi: 10.3390/ma14040915.

[93] "5,10,15,20-Tetrakis-(4-aminophenyl)-porphine-Ni(II)." Accessed: Dec. 21, 2023. [Online]. Available: https://porphyrin-laboratories.com/eng/catalog/Porphine-Base_Eng.php?Land=2&Index=5&Metall=28

[94] "5,10,15,20-Tetrakis-(4-aminophenyl)-porphine-Zn(II)." Accessed: Dec. 21, 2023. [Online]. Available: https://porphyrin-laboratories.com/eng/catalog/Porphine-Base_Eng.php?Synonym=p-TAPP-Zn%28II%29&Name=5,10,15,20-Tetrakis-%284-aminophenyl% 29-porphine-Zn%28II%29&CAS=67595-98-6&Land=2&Index=5&Metall=30

[95] D. H. Apaydin *et al.*, “Synthesis and investigation of tetraphenyltetrabenzoporphyrins for electrocatalytic reduction of carbon dioxide,” *Sustain Energy Fuels*, vol. 2, no. 12, pp. 2747–2753, 2018, doi: 10.1039/c8se00422f.